Magnetic Properties of Electrodeposited Nanocrystalline Ni-Fe Alloys

Magnetic Properties of Electrodeposited Nanocrystalline Ni-Fe Alloys

By

Minghe Wang, B.Sc, M.Sc.

A Thesis

Submitted to the School of Graduate Studies

In Partial Fulfillment of the Requirements

For the Degree

Master of Applied Science

McMaster University

MASTER OF APPLIED SCIENCE (2012) McMaster University

(Materials Science and Engineering) Hamilton, Ontario

TITLE: Magnetic Properties of Electrodeposited Nanocrystalline Ni-Fe Alloys

AUTHOR: Minghe Wang, B.Sc. (JLNU), M.Sc. (JLU)

SUPERVISOR: Professor Marek Niewczas

NUMBER OF PAGES: xiv, 92

To my family and friends

Abstract

Ni-Fe alloys have been used in industrial applications over the past century due to their unique mechanical and magnetic properties. Currently, researchers are interested in enhancing the performance of Ni-Fe alloys by modifying their microstructure. An example of this would be the use of ultra-fine nanocrystalline Ni-Fe alloys for magnetic shielding products that are uniquely shaped and cost effective. These nanocrystalline materials usually exhibit good soft magnetic properties, such as high saturation magnetization, low coercivity and good magnetic permeability. The following study has been devoted to the magnetic properties of electrodeposited nanocrystalline Ni-Fe alloys.

The structure and texture of electrodeposited Ni-Fe alloys was studied by two-dimensional XRD. The Ni-Fe alloys with Fe content from 24.9at. % to 54.2at. % were comprised exclusively of the γ - FCC phase. For 60.2at. % Fe sample, a mixed phase of BCC and FCC structure was found. The lattice parameter increased with increasing Fe content until 54.2at. %, and then decreased due to the presence of BCC structure. The increase in lattice parameter was attributed to the iron replacement of nickel in the Ni crystalline lattice. Texture analysis shows that all Ni-Fe alloys with different Fe content exhibit the fiber texture with a major component of the <100> axis aligned perpendicular to the sample plane. A second component is <111> with a significantly lower volume fraction. It also shows that the Ni-Fe alloy with 44.2at. % Fe exhibits the highest volume fraction of random orientation.

Magnetic measurements showed that all Ni-Fe nanocrystalline alloys exhibit soft magnetic properties with narrow hysteresis loops. The saturation magnetization increased linearly with increasing Fe content. The magnetization at T = 2K were slightly higher than that at T = 298K. The lowest coercivity ∼6Oe was obtained at 44.2 at. % Fe content.

Good agreement between Random Anisotropy Model (RAM) theory and experimental data for all the Ni-Fe alloys has been obtained. By fitting the high field magnetization curve with the Law of Approach to Saturation (LATS), the magnetocrystalline anisotropy constant (K_{eff}) were obtained. K_{eff} decreased with increasing temperature. Also, the ferromagnetic exchange lengths for each Ni-Fe alloy were calculated. They are 26nm, 21nm, 19nm, 18nm, 17nm for Ni-24.9at.%Fe, Ni-33.1at.%Fe, Ni-44.2at.%Fe, Ni-54.2at.%Fe, Ni-60.2at.%Fe at room temperature, respectively. The exchange lengths are larger than the average grain size (D) for all of the samples. The results confirmed the feasibility of Random Anisotropy Model for the prediction of the magnetic properties of the nanocrystalline Ni-Fe alloys fabricated by electrodeposition.

Acknowledgements

I would like to express my deepest gratitude to my supervisor, Prof. Marek Niewczas, for his complete support over the past one and half years of my studies at McMaster. His thoughts and approaches to research were insightful. He taught me many skills in experimental details, data analysis and oral presentations.

I wish to thank Integran Technologies Inc. for providing electrodeposited nanocrystalline Ni-Fe alloys and Ontario Research Fund for funding my research. Special thanks must be given to Dr. James Britton of McMaster Analytical X-Ray Diffraction Facility (MAX) for his support on texture analysis and Dr. Paul of Brockhouse Institute for Materials Research (BIMR) for his support on magnetic properties measurement. I would also like to thank Dr. Gordana Cingara for the TEM images and Dr. Qiuping Bian for his valuable discussion. Sahar Arabi, Fumiaki Hiura, Anna Kula, Xiaohui Jia and Felicia Annor are also thanked for their helpful advice and friendships.

Last but definitely not least, I wish to thank my husband, Songtao Yang, for his love, care and support in both my life and my research; and my parents for their support and encouragement.

Table of Contents

List of Figures

List of Tables

Chapter 1 Introduction and Literature Review

1.1 Magnetism

Magnetism is one of the oldest phenomena known in the history of the natural science. The legend says that the name “magnet” comes from a shepherd called Magnes, who noticed that his iron-nailed shoes or iron-tripped cane stuck to the ground. Regardless what the state of the matter is, amorphous, crystalline, liquid, gaseous, and regardless of what the temperature and pressure conditions are, experiments have shown that all substances are magnets. It is believed that the earliest application of the magnets, called “SiNan” [1], was made in China as presented in Figure 1.1. It is a direction pointer. The spoon is made of magnetic lodestone, and the plate is made of bronze. Its handle pointed to the south. Later in the history, the mariner’s compass was developed by Chinese. Then after more than thousand years, significant progresses were made by several famous people as the big revolution happened in the world of magnetism. William Gilbert realized that the Earth was a giant magnet. Hans Christian Oersted demonstrated that magnetism was related to electricity by bringing a wire carrying an electric current close to a magnetic compass. James Clerk Maxwell established the inter-relationship between electricity and magnetism.

Figure 1.1 Model of the first instrument known to be a compass, called SiNan [2].

Now we know that all mater is made up of atoms. Each atom consists of a very small nucleus composed of protons and neutrons. The central positive nucleus is encircled by moving electrons in orbits (Figure 1.2). The negative charged electrons have orbital and spin angular momentum. Although the mass of a nucleus is significantly larger than that of an electron, the magnetic moment of nucleus is much weaker than the electronic magnetic moment. Therefore, a whole magnet's magnetic moments come from the moments of all of its atoms, and the atomic moments originate from the orbit and spin of electrons.

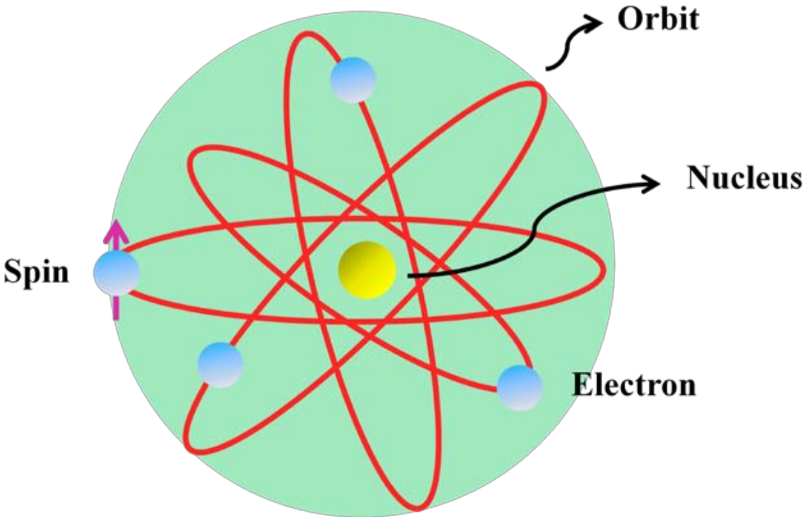

Figure 1.2 Schematics of the electron's motion around the nucleus.

1.1.1 Origin of the magnetism

In an atom, the orbital magnetic moments of some electron pairs cancel each other, as well as spin magnetic moments. The overall magnetic moment of the atom is thus the sum of all of the magnetic moments of the individual electrons. For a completely filled electron shell, the magnetic moments cancel each other out entirely. Therefore, only atoms with partially filled electron shells have a magnetic moment.

Based on the nature and magnitude of the atomic magnetic moments, magnetic materials are classified as:

(I) *Diamagnetic materials*
(II) *Paramagnetic materials*
(III) *Superparamagnetic materials*
(IV) *Antiferromagnetic materials*
(V) *Ferrimagnetic materials*
(VI) *Ferromagnetic materials*

Summary of the temperature dependence of the magnetization, magnetic susceptibility or the reciprocal susceptibility in various types of magnetic materials are presented in Figure 1.3.

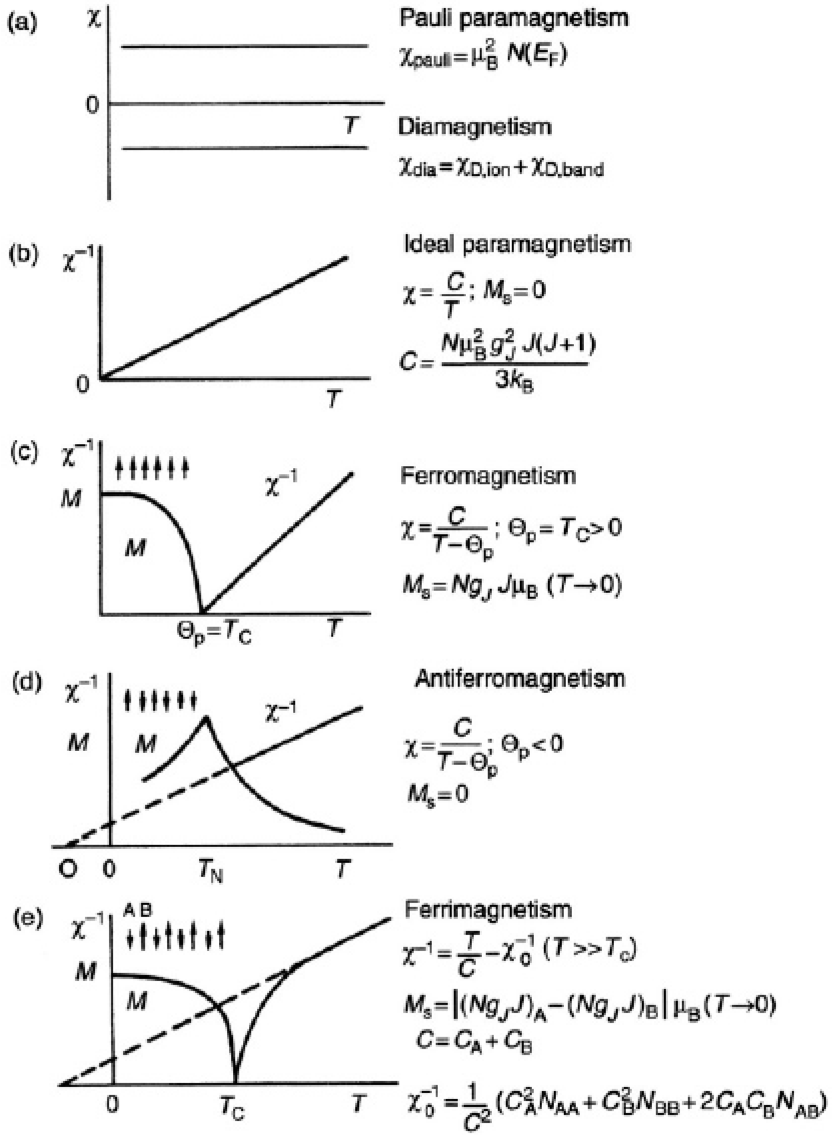

Figure 1.3 The temperature dependence of the magnetization, magnetic susceptibility or the reciprocal susceptibility in various types of magnetic materials [3].

1.1.1.1 Spin and Orbital states of electrons

The states of electrons are characterized by four quantum numbers in Quantum Mechanics. According to the Pauli's principle, it is not possible for two electrons to occupy the same state. In other words, the two electrons cannot have the same sets of the following four quantum numbers.

(I) The total or principal quantum number n (n=1, 2, 3…). Electrons occupying K, L, M… shells are correspond to n=1, 2, 3… respectively.

(II) The orbital angular momentum quantum number l, which can take one of the integral values 0,1,2,3,…, n-1depending on the shape of the orbit. The electrons with l=1, 2, 3, 4…are referred to as s, p, d, f, g…electrons, respectively. For instance, the L shell (n=2) can accommodate s and p electrons.

(III) The magnetic quantum number m_l, which is the component of the orbit angular momentum l along a particular direction (usually along the external magnetic field direction). m_l can take integral values in the ranges between $-l$ to l. For example, for an electron with l equal to 3, the possible values of the angular momentum along a field direction are $2\hbar$, $\hbar$, 0, $-\hbar$, and $-2\hbar$. This is illustrated in Figure 1.4.

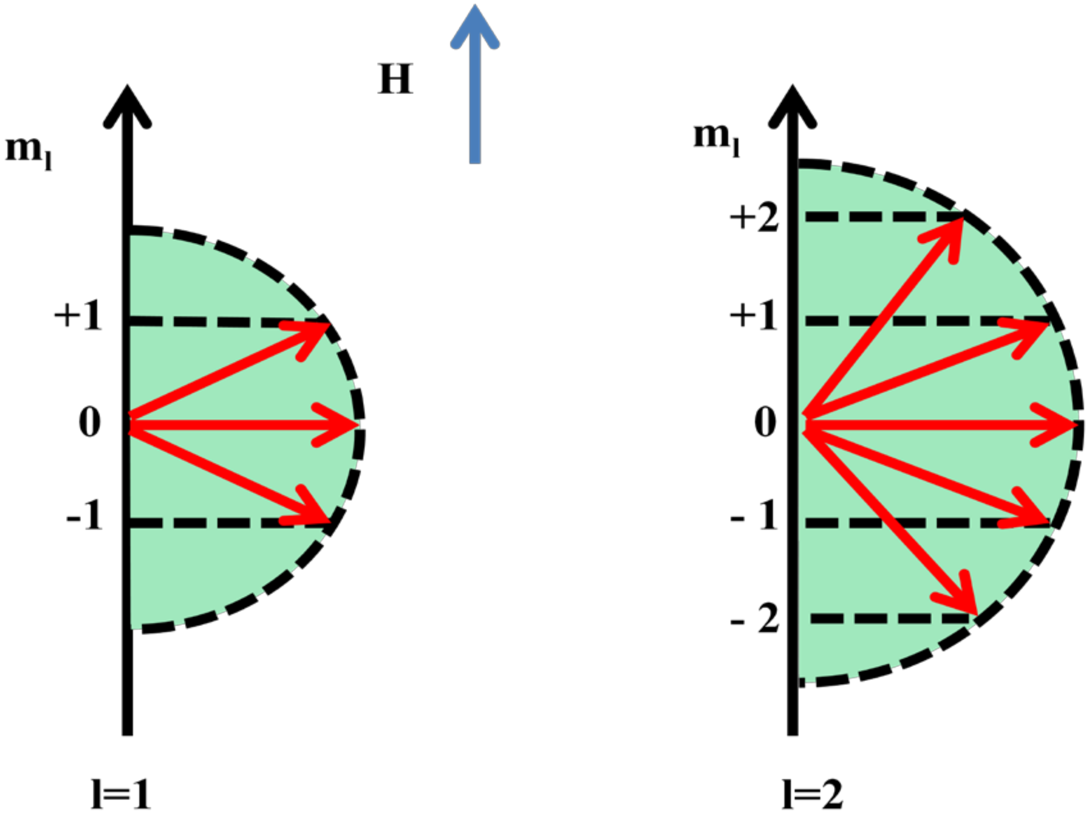

Figure 1.4 Vector model of the orbital angular momentum and magnetic momentum.

(IV) The spin quantum number m_s, which is the component of the electron spin s along a particular direction (e.g. the direction of the external magnetic field). The allowed values of m_s are 1/2 and -1/2, corresponding to the spin angular momentum $\hbar/2$ and $-\hbar/2$.

An electron with an orbital angular momentum $\hbar l$ has an associated magnetic moment

$$\vec{\mu}_l = -\frac{|e|}{2m}\hbar\vec{l} = -\mu_B\vec{l} \tag{1.1}$$

Where μ_B (= 9.27400968(20) $\times 10^{-21}$ Erg/G) is called the Bohr magneton. The absolute value of the magnetic moment is given by

$$|\vec{\mu}_l| = \mu_B\sqrt{l(l+1)} \tag{1.2}$$

And its projection along the direction of the applied field is

$$(\mu_l)_H = -m_l\mu_B \tag{1.3}$$

In the spin angular momentum case, the associated magnetic moment is

$$\vec{\mu}_s = -g\mu_B\vec{s} \tag{1.4}$$

Where $g(= 2.002290716(10))$ is the spectroscopic splitting factor. The component along the field direction is

$$(\mu_s)_H = -gm_s\mu_B \tag{1.5}$$

1.1.1.2 Atomic moments

The total orbital angular momentum of an atom is given by

$$\vec{L} = \sum_i \vec{l}_i \tag{1.6}$$

where the summation extends over all electrons. And the total spin angular momentum is defined as

$$\vec{S} = \sum_i \vec{s}_i \tag{1.7}$$

The total angular momentum of the atom is the sum of the total orbital angular momentum and the total spin angular momentum,

$$\vec{J} = \vec{L} + \vec{S} \tag{1.8}$$

This type of coupling is referred to as Russell-Saunders coupling and it is suitable for the atoms which have an atomic number (Z) smaller than 32. Fe (Z=26) and Ni (Z=28) atoms are both suitable for this rule.

1.1.2 Ferromagnetism

1.1.2.1 Spontaneous magnetization and magnetic domains

For ferromagnetic materials, the magnetization exists in individual regions even in the absence of a magnetic field. This phenomenon is called spontaneous magnetization. The individual regions are magnetic domains, within each of which the local magnetization is saturated but not necessarily parallel. As shown in Figure 1.5, the crystal grains are divided into several domains parallel to its easy magnetization axis, but the magnetization is in alternating directions (red and green areas).

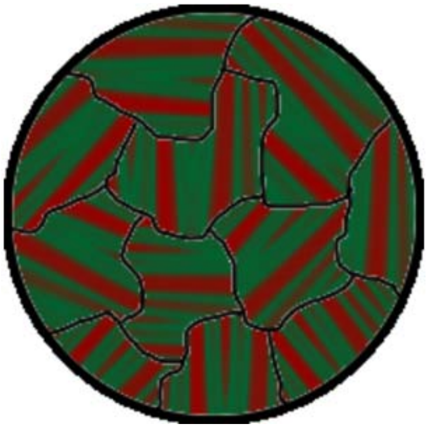

Figure 1.5 Micrograph of surface of ferromagnetic material [4].

To minimize the internal energy, a magnetic material is spontaneously divided into several magnetic domains as shown in Figure 1.6. Case a) shows that the magnetization in the same direction throughout the total volume. Case b) shows that the sample can be split into two domains with the magnetization in opposite directions in each domain to minimize its energy. So, when a domain is too big to be stable, it will divide into smaller domains. The regions between domains are named domain wall which has an average thickness of around 100-150 atoms.

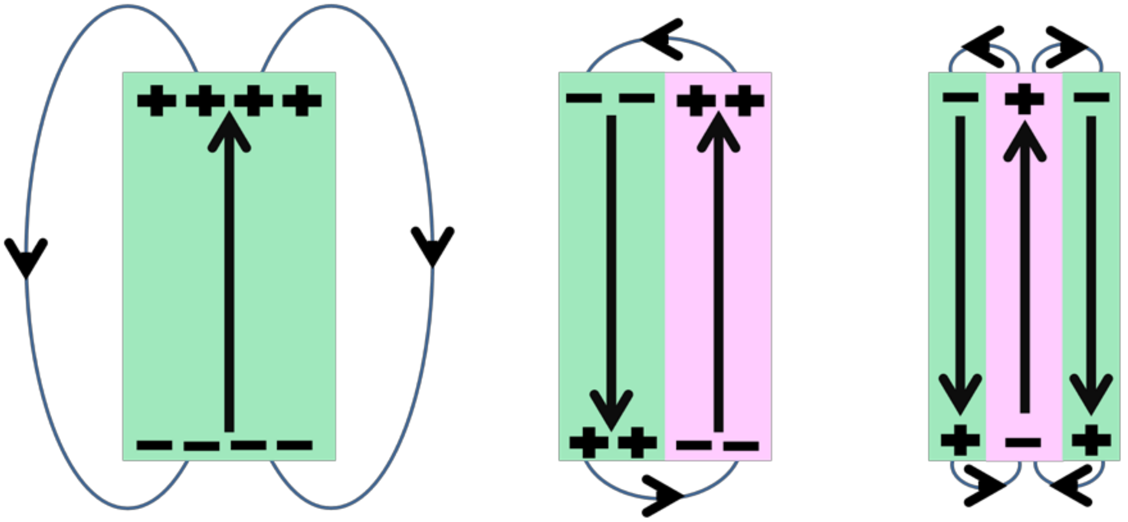

Figure 1.6 Magnetic domain structure in a ferromagnetic material a) single domain, b) and c) multi-domain material.

1.1.2.2 Hysteresis loops and associated materials properties

When a ferromagnetic material is exposed to an external magnetic field, the atomic dipoles align themselves with the field. Even when the magnetic field is removed, part of the dipole alignment will remain. This process is reflected in the existence of the hysteresis between the magnetization of the material and the applied magnetic field. As shown in Figure 1.7, a typical hysteresis loop of ferromagnetic materials shows the relationship between magnetic flux density (B) and magnetizing force (H). The magnetization will follow the dashed line as H is increased until all the magnetic domains are aligned. At this point, the material has approached magnetization saturation. When H is reduced to zero, it can be seen from the hysteresis loop that some magnetic flux remains in the material even at zero H. This point is called the residual flux density. As H is reversed, the flux reduces to zero. This point is called coercivity.

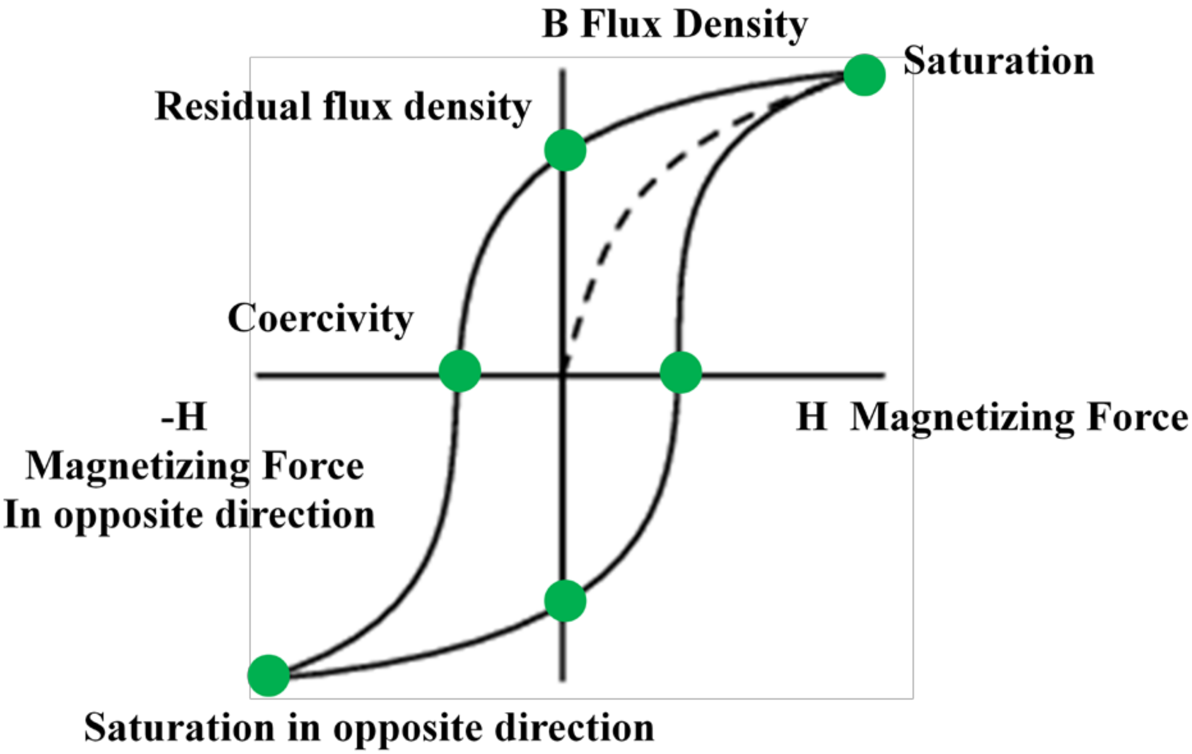

Figure 1.7 Typical hysteresis loop of a ferromagnetic material.

A great deal of information about the magnetic properties can be obtained by studying the properties associated with hysteresis loops, such as the saturation magnetization, coercivity, remnant magnetization , permeability or magnetic susceptibility.

Saturation magnetization: saturation is the state when an increase in applied external magnetic field H cannot increase the magnetization of the material any further [5]. Generally, the magnetization can be related to the temperature by Bloch's law (Equation (1.9)) below the Curie temperature,

$$M(T) = M(0)(1 - BT^{b}) \tag{1.9}$$

where $M(T)$ is the temperature-dependent magnetization, B is the Bloch constant and b is the Bloch exponent. For a three dimensional system, b has been verified to be equal to 3/2[6].

Coercivity: the coercivity of a ferromagnetic material is the intensity of the applied magnetic field required to reduce the magnetization of that material to zero after the magnetization of the sample has been driven to saturation [7]. Ferromagnetic materials with high coercivity and low coercivity are called magnetically hard materials and soft materials, respectively.

Remnant magnetization: Remanence is the magnetization left behind in a ferromagnetic material after an external magnetic field is removed. It is responsible for the magnetic memory in magnetic storage devices [8].

Magnetic susceptibility: all the materials can be magnetized in the presence of an applied magnetic field, altering the applied field. This property is called magnetic susceptibility [9]. The magnetic susceptibility is defined as the ratio of the intensity of magnetism induced in material to the applied magnetic field. It is a dimensionless proportionality constant.

Permeability: permeability describes the ease with which a magnetic flux is established in the material. The permeability for 99.8% pure Ni, Fe and permalloy are 1.25×10^{-4} H/m, 6.28×10^{-3} H/m, and 1.0×10^{-2} H/m, respectively.

1.1.2.3 Magneto-crystalline anisotropy

Magneto-crystalline anisotropy is referred to the dependence of the internal energy on the crystallographic orientation of the magnetized crystal. It can be most easily seen through magnetization curves along different crystal directions. As shown in Figure 1.8, at room temperature, the easy magnetization direction of FCC Ni is <111>, and the hard magnetization direction is <100>. However, for BCC Fe, the easy and hard magnetization directions are <100> and <111>, respectively.

The magneto-crystalline anisotropy is an intrinsic property of ferromagnetic materials. It arises mostly from the spin-orbit coupling which is very weak compared to the exchange interactions between two or more identical particles [10]. The crystallographic anisotropy energy of a cubic crystal can be described by

$$E_a = K_0 + K_1(\alpha_1^2\alpha_2^2 + \alpha_2^2\alpha_3^2 + \alpha_3^2\alpha_1^2) + K_2(\alpha_1^2\alpha_2^2\alpha_3^2) + \cdots \tag{1.10}$$

Where α_i ($i = 1, 2, 3$ ...) are the cosines between the direction of magnetization and the crystal axes. K_0, K_1 and K_2 are the cubic anisotropy constants.

At room temperature, for BCC Fe, $K_1 = 4.2 \times 10^4 J/m^3$ and $K_2 = 1.5 \times 10^4 J/m^3$. On the other hand for FCC Ni, $K_1 = -4.5 \times 10^3 J/m^3$ and $K_2 = 2.34 \times 10^3 J/m^3$. Generally, the magnitudes of the anisotropy constants decrease rapidly with increasing temperature below Curie temperature.

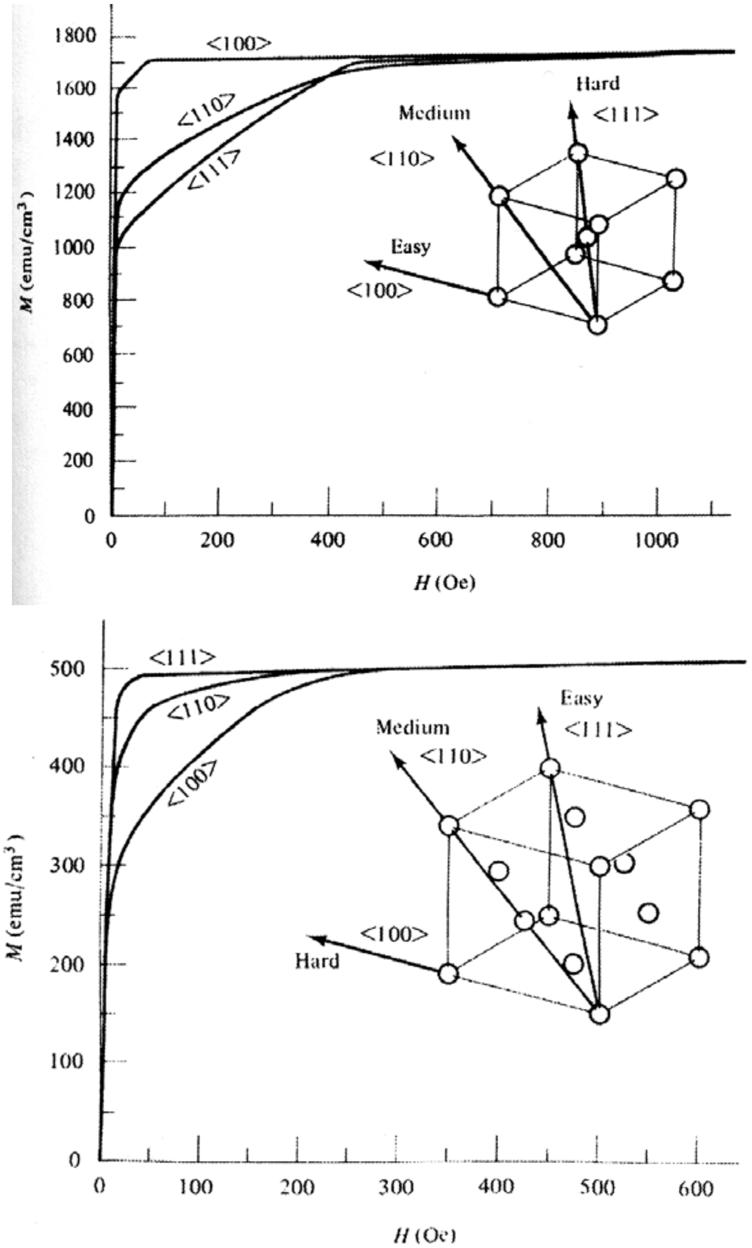

Figure 1.8 Magnetization curves for single crystal of Iron (a) and Nickel (b) along different crystallographic directions [65].

1.1.3 Law of Approach to Saturation (LATS)

Generally, a whole hysteresis loop is difficult to simulate because of the complex magnetic interactions between grains interiors and grain boundaries which makes the demagnetization process difficult to be described accurately. The law of approach to saturation is one of the effective ways to simulate part of the hysteresis loop. In principle the law of approach to saturation can be applied to all the magnetic materials. However, for some types of the materials, a critical verification of the theory with the experiment is necessary. By fitting the magnetization curves using the law of approach to saturation, the saturation magnetization and magneto-crystalline anisotropy constant K_1 (effective magneto-crystalline anisotropy constant K_{eff} for nanocrystalline materials) can be obtained. Thus, it is very important to model the magnetization process with the law of approach to saturation. The law of approach to saturation is expressed mathematically by the simple formula

$$M = M_s\left(1 - \frac{a_1}{\sqrt{H}} - \frac{a_2}{H^2} - \frac{a_3}{H^3} \dots\right) + \chi_{hf} H \tag{1.11}$$

Where α_i ($i = 1, 2, 3 \dots$) are related to different processes during magnetization. Kronmüller [11] has demonstrated that the main contributions in Equation (1.11) are coming from $\frac{1}{\sqrt{\mathrm{H}}}$ and $\frac{1}{\mathrm{H}^2}$ terms.

$\frac{a_1}{\sqrt{H}}$ term is known as the magnetic hardness. It arises from the local stress caused by the structural defects [12, 13], nonmagnetic inclusions and the leakage field from ferromagnetic materials [14]. However, the theoretical explanation is still controversial. There is no explanation that has been fully accepted so far.

$\chi_{hf}H$ term is often referred to as paramagnetism-like term. Therefore, χ_{hf} is the magnetic susceptibility for the paramagnetic (parallel) process. In general, this term could be ignored when the magnetic field is not strong enough.

$\frac{a_2}{H^2}$ term: The term $\frac{1}{\mathrm{H}^2}$ is attributed mainly to the non-compensated anisotropy energy. When the external magnetic field is strong enough, each grain is magnetized by rotating magnetic domains. If we assume the angle between the applied magnetic field and the magnetization M is θ, which is determined by the minimum total energy in the approach to saturation process, then, the magnetization along the direction of the magnetic field H is

$$M = M_s cos\theta = M_s(1 - sin^2\theta)^{\frac{1}{2}} = M_s\left(1 - \frac{\theta^2}{2} + \frac{\theta^4}{24} \cdots\right) \qquad (1.12)$$

In the stage of approaching to saturation, the demagnetization field energy and the exchange coupling energy are ignored when calculating the total energy. Two energies related to the domain rotation, the magneto-crystalline anisotropy energy (E_K) and the external field energy (E_H), are important. Therefore, the total energy could be written as:

$$E = E_K + E_H = E_K - \mu_0 H M_s cos\theta \tag{1.13}$$

Since $\left(\frac{\partial E}{\partial \theta}\right) = 0$,

$$\frac{\partial E_K}{\partial \theta} + \mu_0 H M_s sin\theta = 0 \tag{1.14}$$

Since θ is very small, and $sin\theta \cong \theta$,

$$\theta = -\frac{1}{\mu_0 H M_s}\frac{\partial E_K}{\partial \theta} \tag{1.15}$$

Comparing with Equation (1.11),

$$a_2 = \frac{1}{2\mu_0^2 M_s^2}(\frac{\partial E_K}{\partial \theta})^2 \tag{1.16}$$

For cubic crystal structures, a_2 is given by

$$a_2 = \frac{8}{105}\frac{K_1^2}{M_s^2 \mu_0^2} \tag{1.17}$$

By fitting the high field magnetization curve with the law of approach to saturation, the factors in the Equation (1.11), a_1, a_2 and χ_{hf} can be determined. Furthermore, for nanocrystalline materials, the effective magneto-crystalline anisotropy constant can be deduced [15-19],

$$K_{eff} = \mu_0 M_s \sqrt{\frac{105 a_2}{8}} \tag{1.18}$$

Where μ_0 is the vacuum magnetic permeability ($4\pi \times 10^{-7}\ Hm^{-1}$). By fitting the high-field magnetization curve using equation (1.11) with least square method, a_2 values can be obtained for nanocrystalline Ni-Fe alloys with different Fe content, and then the effective magneto-crystalline anisotropy can be calculated.

1.1.4 Random Anisotropy Model

Soft magnetic properties have been observed in various amorphous or nanocrystalline [37- 38] systems. Alben, Becker, and Chi [20] have described the effective anisotropy energy of the amorphous materials by random anisotropy model, and the effective anisotropy energy density in this model is given by the square root of the mean-square fluctuation of the anisotropy energy in the exchange coupled volume. Herzer [21] first applied the Random Anisotropy Model (RAM) to nanocrystalline Fe-Si-B-Nb-Cu to understand the origin of the soft magnetic properties in this system. Since then, this model has been employed widely to explain the origin of the soft magnetic properties in various nanocrystalline materials [22-23]. Within the random anisotropy model, when the grain size is larger than the exchange length, the magnetization is determined by the local magnetocrystalline anisotropy energy. However, if the grain size is smaller than the exchange length, the magnetic moments will be more and more aligned parallel to each other resulting in the effective anisotropy being averaged over several structural units and therefore being reduced in magnitude (Figure 1.9).

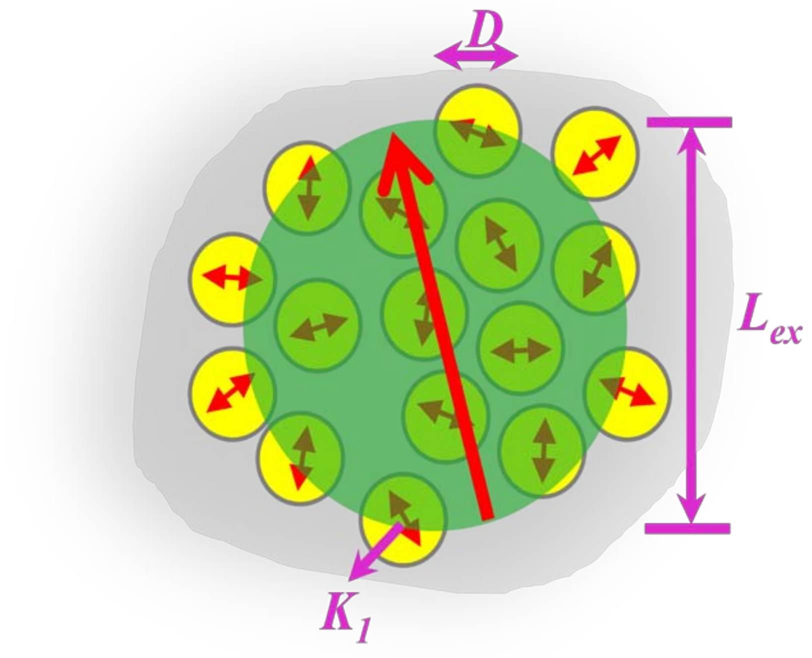

Figure 1.9 Schematics showing length scales used in Random Anisotropy Model.

According to the Random Anisotropy Model, when the average grain size is much smaller than the exchange length, the exchange length can be related to the effective magnetocrystalline anisotropy by Equation 1.19,

$$L_{ex} = \varphi_0 \sqrt{\frac{A}{K_{eff}}} \tag{1.19}$$

Where A is the exchange stiffness, K_{eff} is the effective magnetic anisotropy constant and φ_0 is proportionality factor in the order of one. For Fe-based alloys, L_{ex} is about 20~40nm, and for Co-based alloys, L_{ex} is about 5~10nm. Since the average grain size for the amorphous and nanocrystalline alloys are within atomic scale range below 20nm, the magnetization behaviour in both the amorphous and nanocrystalline alloys can often be described by the Random Anisotropy Model.

The effective magnetocrystalline anisotropy can also be written as

$$K_{eff} = K_1^4 * D^6 / A^3 \tag{1.20}$$

which indicates that the effective magneto-crystalline anisotropy can be related to the grain size. As a result, a relationship between the coercivity and initial permeability and the grain size can be established because of their relationship with effective magneto-crystalline anisotropy. As a consequence, the coercivity and the permeability will vary with the grain size, as shown in Figure 1.10.

$$H_c = p_c \frac{K_{eff}}{M_s} \sim p_c \frac{K_1 D^6}{M_s A^3} \tag{1.21}$$

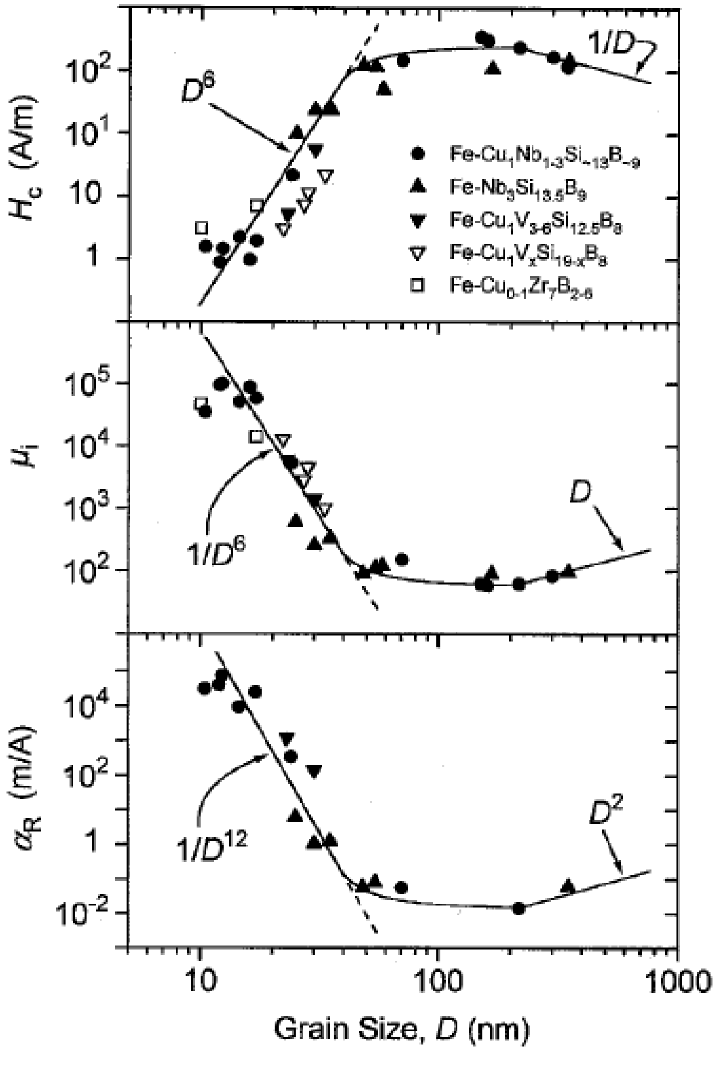

Figure 1.10 Coercivity and initial permeability versus the average grain size in different Fe-based alloys [24].

1.2 Nanocrystalline materials

1.2.1 Structure of nanocrystalline metal electrodeposits

Nanocrystalline materials made by numerous synthesis techniques were first reported in early 1980s. They exhibit an atomic structure which differs from the crystalline state (with long-range order) and the glass state (with short range order). They are single phase or multiphase polycrystals with grain size in the order of a few nanometers. Figure 1.11 presents the hard sphere model of a nanocrystalline material. The boundary atoms are represented by the open circles can be distinguished from the lattice atoms represented by the full circles. The atoms in the grain boundaries are also assumed to be chemically identical to each other since they separate different orientation of individual crystals (grain interiors).

The main difference between conventional electrodeposits and the nanocrystalline deposits is the grain shape anisotropy. A structure transition from fine-grained-equiaxed to coarse-grained columnar structure with strong grain shape anisotropy arises from the increasing of the thickness of conventional electrodeposits. On the other hand, the nanocrystalline deposits can be grown to any thickness without grain shape anisotropy under a favourable nucleation controlled electrodeposition conditions. Typically, the electrodeposition of nanocrystalline materials is performed under the nonequilibrium conditions, resulting in the small grain size of electrodeposits. Consequently, a large volume fraction of grain boundaries can be obtained. For a boundary thickness of 1nm, an intercrystalline volume fraction of 50% can be achieved at grain size smaller than 5nm.

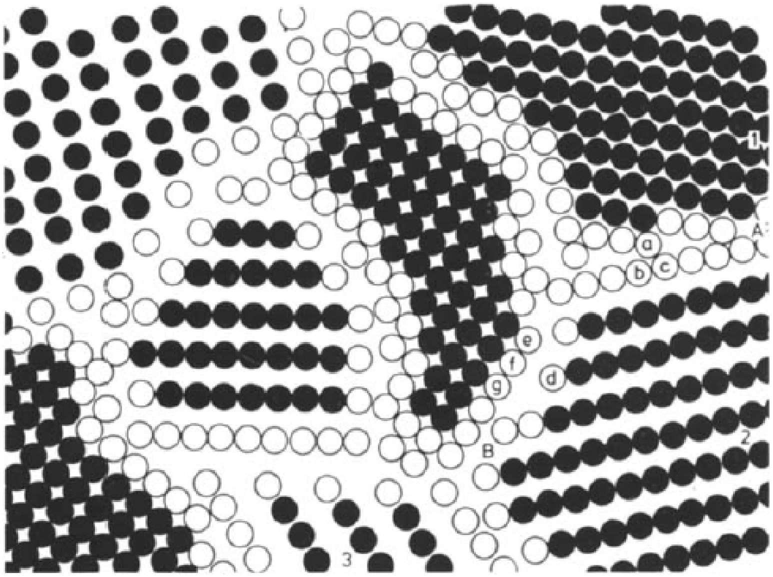

Figure 1.11 Schematic representation of a nanocrystalline material consisting of the atoms associated with the grain interiors (full circles) and those constituting the grain boundary network (open circles) [25].

1.2.2 Soft magnetic properties of nanocrystalline materials

Depending on the difficulty of demagnetizing a magnetic material, ferromagnetic materials can be categorized into two types: soft magnetic materials and hard magnetic materials. In soft magnetic materials, the demagnetization state can be achieved at low magnetic field. In contrast, a high magnetic field is required to demagnetize hard magnetic materials. Nanocrystalline materials usually exhibit soft magnetic properties. Two important parameters of ferromagnetic materials in the magnetization process are saturation magnetization and coercivity. For nanocrystalline materials, initial studies have revealed that saturation magnetization reduced greatly with decreasing the grain size. A 40% decrease in saturation magnetization for nanocrystalline iron with 6nm grain size compared to bulk polycrystalline was first reported by Gleiter [26]. Yao and coworkers [27] and Krill and coworkers [28] also found that there is a strong relationship between the saturation magnetization and the grain size. In contrast, Aus and co-workers [29] studied the magnetic properties of Ni with grain size varying from 10μm down to 10nm, and observed that saturation magnetization was only 10% less than for conventional polycrystalline Ni. These results are consistent with the calculations which considered the structural disorder by introducing the grain boundaries. The boundaries ranged from Σ3 with minimum structure disorder, Σ5, Σ13 to amorphous boundaries with maximum structure disorder. The calculation results show that even for the amorphous materials, the average moment was only reduced by 15%. Daroczi et al., Szpunar et al. and Cheung et al. have recently reported their findings confirming that the disorder grain boundary has an insignificant effect on saturation magnetization [60-62]. In terms of coercivity, it was discussed that the nanocrystalline alloys follow the D^6 relationship predicted by Random Anisotropy Model. Experiments have shown that by controlling the grain size, very low coercivity can be obtained.

1.2.3 Applications of electrodeposited nanocrystalline Ni-Fe alloys

Numerous practical applications for nanocrystalline materials are based upon their unique properties, such as high strength and soft magnetic properties. Table 1.1 displays the mechanical properties of conventional and nanocrystalline nickel. The grain sizes are 10-100 nm and 10 µm for nanocrystalline and conventional polycrystalline Nickel (99.99%), respectively. Remarkable increase in yield strength, ultimate tensile strength and hardness has been obtained by decreasing the grain size to nano scale [30]. The unique mechanical properties make nanocrystalline materials a good candidate for many micro-electromechanical systems (MEMS), the use of electrodeposited nano structural MEMS devices would improve the reliability of the devices. In addition, the increased strength of Ni-Fe alloys can improve the overall performance, such as the specific strength, the elastic energy storage capacity and the thermal shock resistance.

Table 1.1 Mechanical properties of conventional and nanocrystalline nickel [30].

Property	Ni 10µm	Ni 100nm	Ni 10nm
Yield Strength, MPa (25°C)	103	690	>900
Ultimate Tensile Strength, MPa (25°C)	403	1100	>2000
Tensile Elongation, % (25°C)	50	>15	1
Elongation in Bending, % (25°C)	-	>40	-
Modulus of Elasticity, GPa (25°C)	207	214	204
Vickers Hardness, kg/mm^2	140	300	650
Work Hardening Coefficient	0.4	0.15	0.0
Fatigue Strength, MPa (10^8 cycles/air/25°C)	241	275	-
Wear Rate (dry air pin on disc),µm^3/µm	1330	-	7.9
Coefficient of Friction (dry air on disc)	0.9	-	0.5

Fe-and Co- based soft magnetic materials with grain size in nano scale are used in industry, however, the production techniques of the amorphous precursor alloys require substantial alloying with metalloids, which decreases the saturation magnetization. As shown in Figure 1.12, in the case of electrodeposited nanocrystalline alloys, the saturation magnetization is not sacrificed [31].

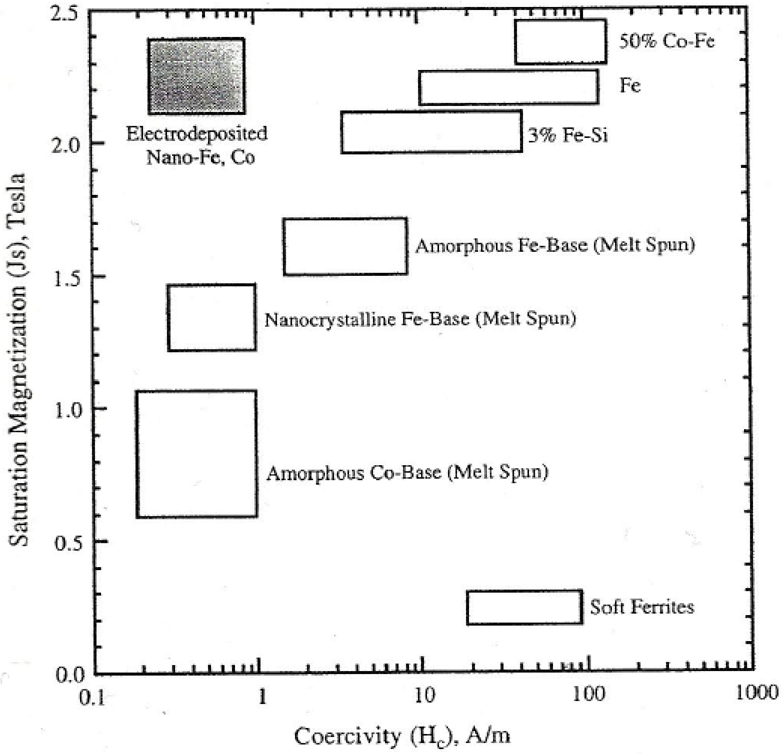

Figure 1.12 Saturation magnetization as a function of coercivity for electrodeposited materials (grey box) along with various commercial materials (white boxes) [31].

Due to the unique mechanical and magnetic properties, the Ni-Fe alloys with different Fe content have been used in industrial applications for over hundred years [32-36]. For example, they have been uses as thermostatic bimetals, glass sealing, integrated circuit packaging, cathode ray tube shadow masks, electromagnetic shielding, read-write heads, high efficiency motors or emerging microelectro mechanical system components. The Ni-22% Fe alloy called permalloy is the most well-known of these alloys. Permalloy is notable for its high magnetic permeability, low coercivity, near zero magnetostriction and significant anisotropy magnetoresistance. The electrodeposited nanocrystalline permalloy with grain size of approximately 11nm has shown an excellent soft magnetic property and a microhardness approaching 900 VHN [37].

Chapter 2 Objectives and Structure of the Thesis

2.1 Objectives of the research

Due to the fact that Fe is stronger ferromagnetic element than Ni, it is expected that better soft magnetic properties can be achieved by increasing the iron content in Ni-Fe binary system. The overall objective of this work is to develop a better understanding of the relationship between composition, microstructure and the magnetic properties of electrodeposited nanocrystalline Ni-Fe alloys between 2K and 298K. The specific objectives of this research include:

1. To determine the structure and texture of electrodeposited nanocrystalline Ni-Fe alloys by 2D-XRD.
2. To calculate the pole figures and crystalline volume fractions for all the Ni-Fe alloys, and correlate texture with the alloy composition.

3. To investigate the magnetic properties of nanocrystalline Ni-Fe alloys with different Fe content, and correlate the saturation magnetization and coercivity with the alloy composition.
4. To estimate the effective magnetocrystalline anisotropy constant K_{eff} by fitting the high field magnetization curve using Law of Approach to Saturation.
5. To estimate the exchange length of all nanocrystalline Ni-Fe alloys by using the Random Anisotropy Model and to assess the applicability of Random Anisotropy Model for prediction of magnetic properties of nanocrystalline Ni-Fe alloys.

2.2 Thesis outline

The thesis is organized as follows:

Chapter 1 provides the background information of this research, including the basic concepts of magnetism of nanocrystalline materials and related literature review. The specific objectives and an outline of the thesis are also presented herein.

Chapter 2 describes the objectives and structure of the thesis.

Chapter 3 describes the experimental procedure and instrumentation used.

Chapter 4 describes the results of the investigation of the structure, texture and magnetic properties of the electrodeposited nanocrystalline Ni-Fe alloys and provides discussion of the results.

Chapter 5 summarizes the main conclusions and contributions of this project, and proposes plan for the future research.

Chapter 3 Materials and Methodology

3.1 Materials

Nanocrystalline Ni-x wt. % Fe (x=24, 32, 43, 53, 59) alloys were provided by Integran Technologies Inc. The alloys were fabricated by electrodeposition technique. All the samples were in the form of foils with nominal thickness of about 50µm. Circular disks (3mm diameter) cut from the foils were used to characterize the texture and magnetic properties.

The Weight Percent can be converted to Atomic Percent as presented in Table 3.1. As shown in Table 3.1, there are no big differences between the Weight Percent and the Atomic Percent for all samples because the relative atomic weight for Fe and Ni are 55.845 and 58.6934, respectively.

Table 3.1 Conversion of weight percent to atomic percent in Ni-Fe alloys.

wt.% Fe	at.% Fe
24	24.9
32	33.1
43	44.2
53	54.2
59	60.2

3.2 Two-dimensional X-ray diffraction

3.2.1 Structure characterization

Structure analysis of the nanocrystalline Ni-Fe alloys were conducted under room temperature by Brukers Smart6000-D8 diffractometer (CuK$_\alpha$, λ=0.154nm). In order to improve the accuracy of the measurements, three different scans were done on the samples with detector-sample distance of 4.9 mm. The scans were done at $2\theta = 36^o$, $\omega =$

198^o, 2θ = 60^o, ω = 210^o, and 2θ = 84^o, ω = 222^o with scanning time of 300 seconds, respectively. The three frames recorded from experiments were further combined using the software FrmUtility and Bulk Rename Utility. The transferred frames can be loaded to TOPAS software for structure determination.

Grain size was calculated based on the Scherrer equation (Equation 3.1),

$$\tau = \frac{K\lambda}{\beta cos\theta} \tag{3.1}$$

Where τ is the mean grain size for nanocrystalline material, K is the shape factor, the dimensionless shape factor has a typical value of about 0.9, λ is the X-ray wavelength, β is the line broadening at half the maximum intensity (FWHM) in radians, and θ is the Bragg angle [38].

3.2.2 Texture characterization

Most of the crystallites have preferred orientation or a texture. Pole figure is a useful technique to determine the orientation distribution of sample's crystallites. When a conventional X-ray diffractometer is used for texture measurement, the crystallite orientation distribution is measured in one direction at a time, therefore, full texture information must be achieved by rotating the sample to all orientations. However, for two-dimensional X-ray diffraction systems, the orientation distribution of several crystallographic planes over a range of angles can be measured simultaneously. The texture of all the electrodeposited nanocrystalline Ni-Fe alloys with different Fe content were evaluated using a Bruker Smart6000-D8 diffractometer with parallel-focused CuKα ($\lambda = 0.154$ (nm)) radiation (Rigaku RU-200-rotating anode, 50kV/90mA), collected at an 8 cm distance using an area detector. Raw diffraction data was then used to create pole figures ($0 \leq \varphi \leq 360°$ and $0 \leq \psi \leq 82°$) using the GADDS software package, for (111), (200), and (220) reflections. Finally, the orientation distribution function was calculated with the MATLAB-MTex software package. Following this the recalculated pole figures were created.

3.3 Superconducting Quantum Interference Device (SQUID)

The SQUID (Superconducting Quantum Interference Device) is one of the most sensitive magnetic flux detectors known. It is sensitive enough to measure field as low as 10^{-18} T. The basic components of a SQUID system usually include Flux-Locked Loop, Cryogenic Dewar, Cryogenic Cable or Probe, SQUID sensor, Field Sensing Coil, Data Acquisition system and Control Electronics [39].

SQUID uses a combination of the properties of electron-pair wave coherence and Josephson Junctions to detect magnetic fields. The Josephson Junctions is a ring of superconducting material with one or more weak links shown in Figure 3.1. With weak-links at point W and X whose critical current, i is much less than the critical current of the main ring. This produces a very low current density making the momentum of the electron-pairs small. The wavelength of the electron-pairs is thus very long leading to little difference in phase between any parts of the ring [63].

If a magnetic field B is applied perpendicular to the plane of the ring, a phase difference is produced in the electron-pair wave along the path XYW and WZX. One of the features of a superconducting loop is that the magnetic flux ϕ, passing through it which is the product of the magnetic field and the area of the loop and is quantized in units of $\phi_0=hl(2\theta)$, where h is the Planck's constant, 2θ is the charge of the Cooper pair of electrons, and ϕ_0 has a value of $2x10^{-15}$ tesla m^2. If there are no obstacles in the loop, then the superconducting current will compensate for the presence of an arbitrary magnetic field so that the total flux through the loop is a multiple of ϕ_0 [63].

The SQUID has two such Josephson junctions, a Input Coil and a Pickup Coil. The Input Coil couples external flux into the SQUID, and the Pickup Coil couples currents into the Input Coil. The coupled currents generate flux that couples into the SQUID loop and are detected by the SQUID.

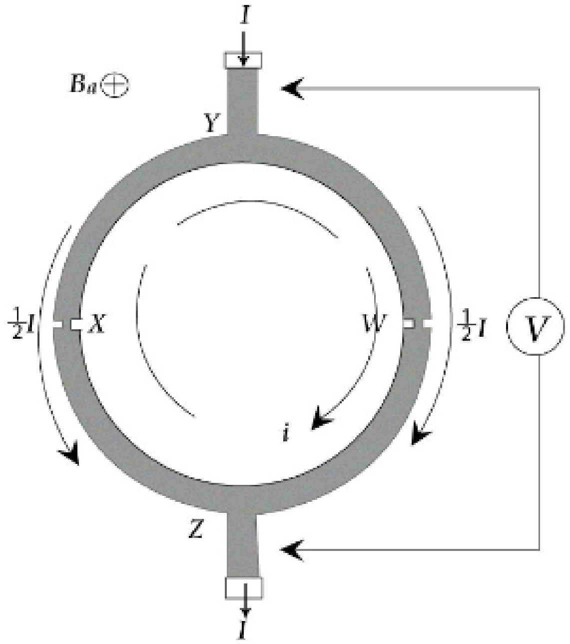

Figure 3.1 Superconducting Quantum Interference Device as a simple magnetometer [64].

Magnetic properties of electrodeposited nanocrystalline Ni-Fe alloys were measured by SQUID magnetometer system with the magnetic field up to ± 4T at 2K and 298K, applied parallel and perpendicular to the sample plane (Figure 3.2).

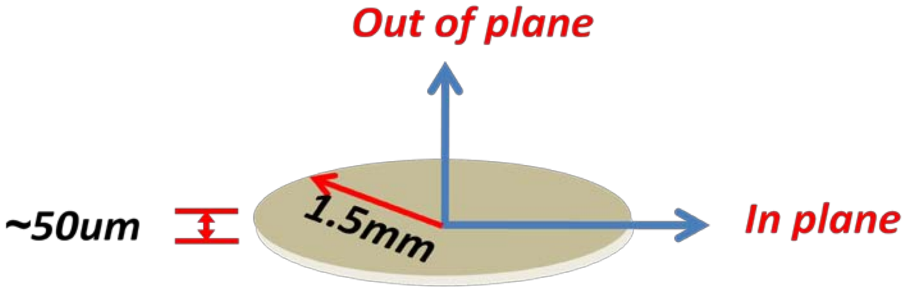

Figure 3.2 Schematics of the magnetic measurements with the sample plane parallel and perpendicular to the applied magnetic field.

Chapter 4 Results and Discussion

4.1 Structure determination and texture analysis

4.1.1 Structure determination

The XRD patterns of Ni-Fe alloys with different Fe content are shown in Figure 4.1. As expected, for Fe content from 24.9 to 54.2 at. %, their diffraction peaks correspond entirely to γ-FCC phase. The peaks corresponding to (111) reflection at 2θ=43.8-44.1, (200) at 2θ=50.97-51.3, and (220) were observed for all the samples with different Fe content. For 60.2 at. % Fe sample, mixed phases of BCC and FCC structure were observed. This result is consistent with the Fe-Ni phase diagram shown in Figure 4.2. According to the phase diagram, as Fe content increases, the BCC phase emerges from about 54.2 wt. % Fe and becomes the predominant phase in the alloys. However, the peaks intensities were changed as compared to the standard. This could be attributed to the presence of the preferred orientations. The preferred orientations are (111), (200) and (220) reflections for FCC, and (110) reflections for BCC. Diffraction peaks arising from Ni or Fe oxides were not observed in any sample.

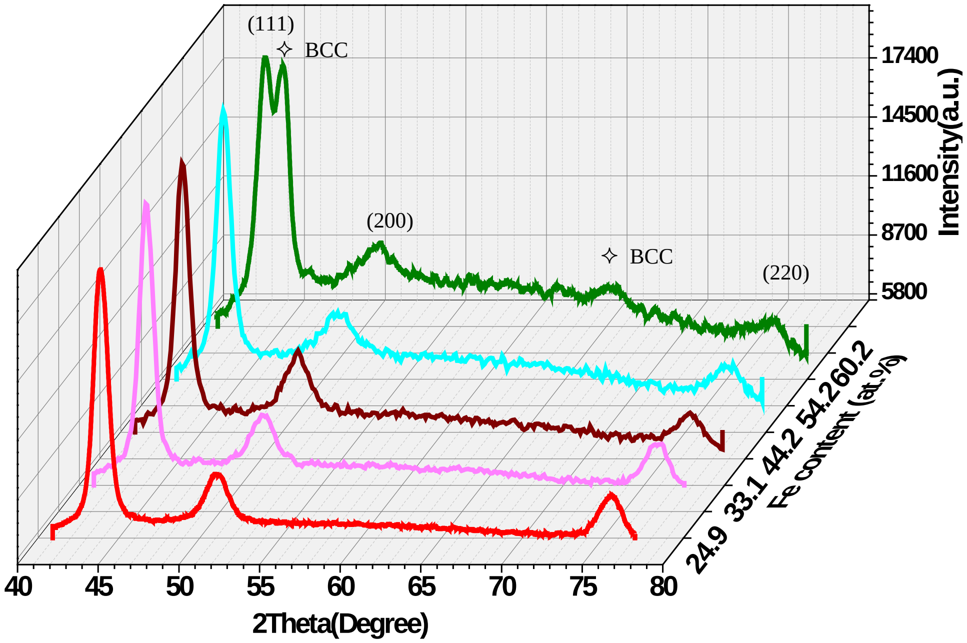

Figure 4.1 XRD patterns of Ni-x at. % Fe alloys with Fe content of 24.9, 32.1, 44.2, 54.2, and 60.2 at.%.

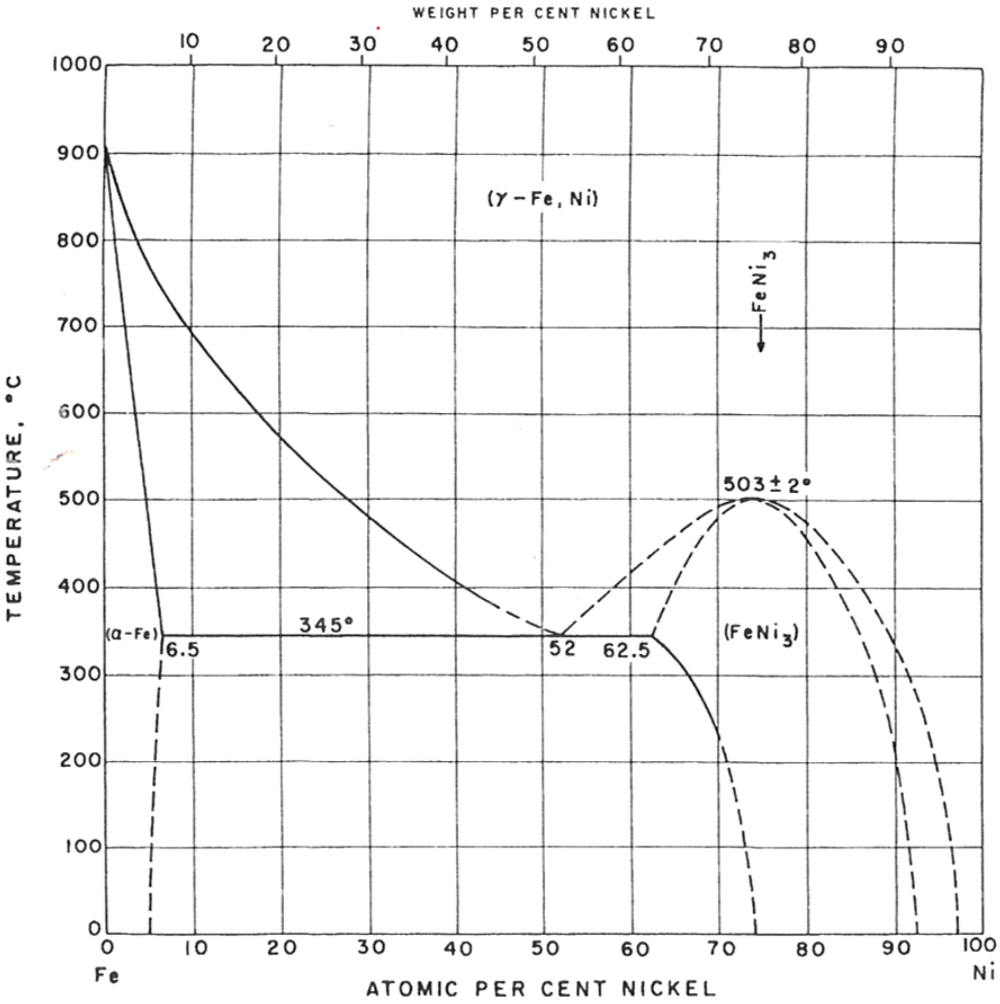

Figure 4.2 Equilibrium phase diagram of Fe-Ni alloys [40].

The XRD pattern also confirmed that all the alloys are solid solutions, in which Fe is dissolved in Ni, changing the lattice parameters. The lattice parameters were calculated by converting the average atomic plane spacing of the (111) planes ($a_{FCC1} = \sqrt{3}d_{(111)}$), (200) planes ($a_{FCC2} = 2d_{(200)}$) and (220) planes ($a_{FCC3} = 2\sqrt{2}d_{(220)}$) for all the nanocrystalline Ni-Fe alloys. As shown in Figure 4.3, the lattice parameter of FCC increases linearly with increasing Fe content until 54.2at. %, and then decreases due to the presence of Fe-rich BCC structure. The lattice parameters values are comparable to the values obtained in previous studies by Hongqi Li et al [41].

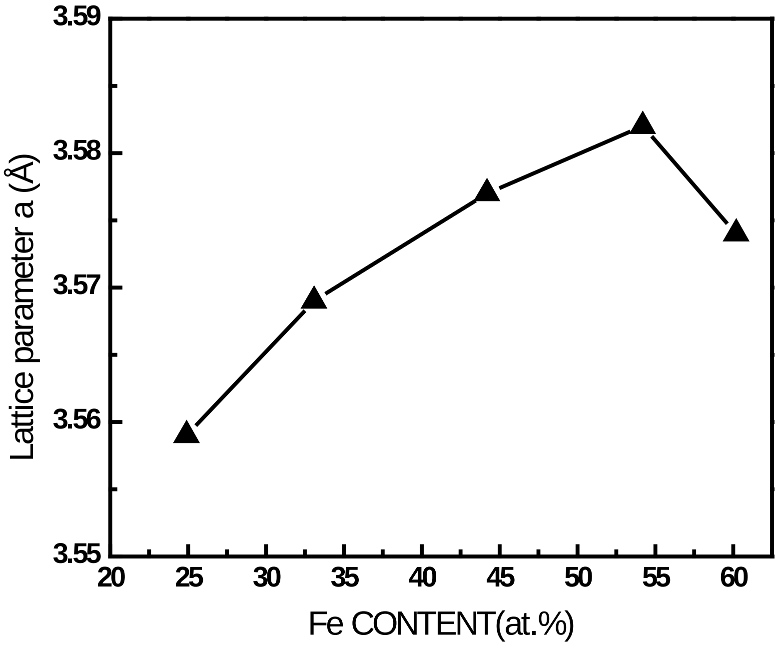

Figure 4.3 Lattice parameter as a function of the Fe content in electrodeposited nanocrystalline Ni-Fe alloys.

The grain size was estimated using the (111) peak of FCC phase by means of the Scherrer formula. In Figure 4.4, the grain size is plotted against the Fe content. The grain size results are comparable with those obtained with TEM methods. The XRD measurements indicate all the electrodeposited Ni-Fe alloys with different Fe content have nanocrystalline grain structure. With the Fe content in the range from 24.9-54.2at. %, the grain size remains approximately constant (~10nm). When the Fe content increases to

60.2at. %, the grain size decreases to 8nm due to the presence of the mixed phases of BCC and FCC. This is consistent with the previous study which reported that the mixed structure exhibited a smaller grain size than either FCC or BCC alloys [42].

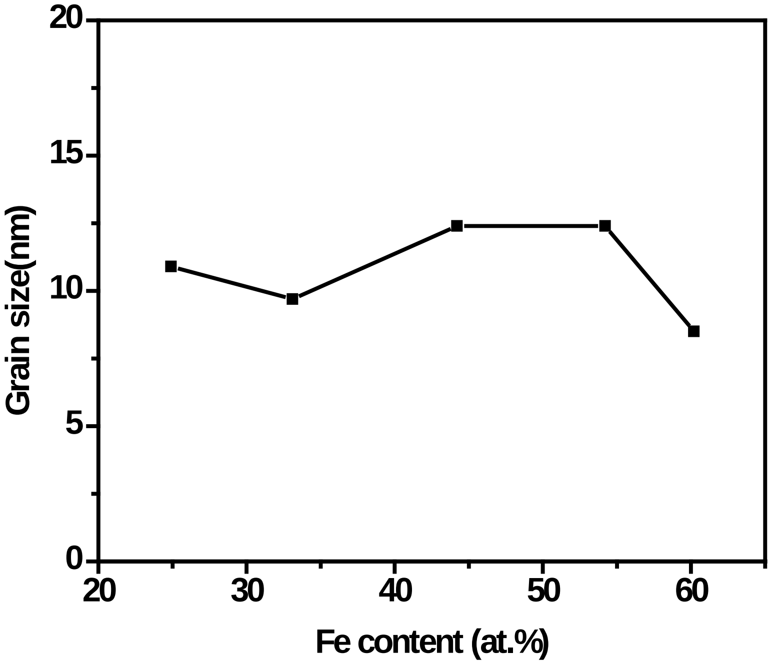

Figure 4.4 Grain size as a function of the Fe content in nanocrystalline Ni-Fe alloys.

4.1.2 Texture analysis

In order to determine the crystallographic texture, pole figures in a full range of hkl angles were recalculated based on the orientation distribution function (ODF). As shown in Figure 4.5, all the electrodeposited nanocrystalline Ni-Fe alloy samples with different Fe content exhibit the fiber texture with a major component of the <100> axis perpendicular to the sample plane. A second component is <111> with a significantly lower strength. The third component is <110> with a very low strength.

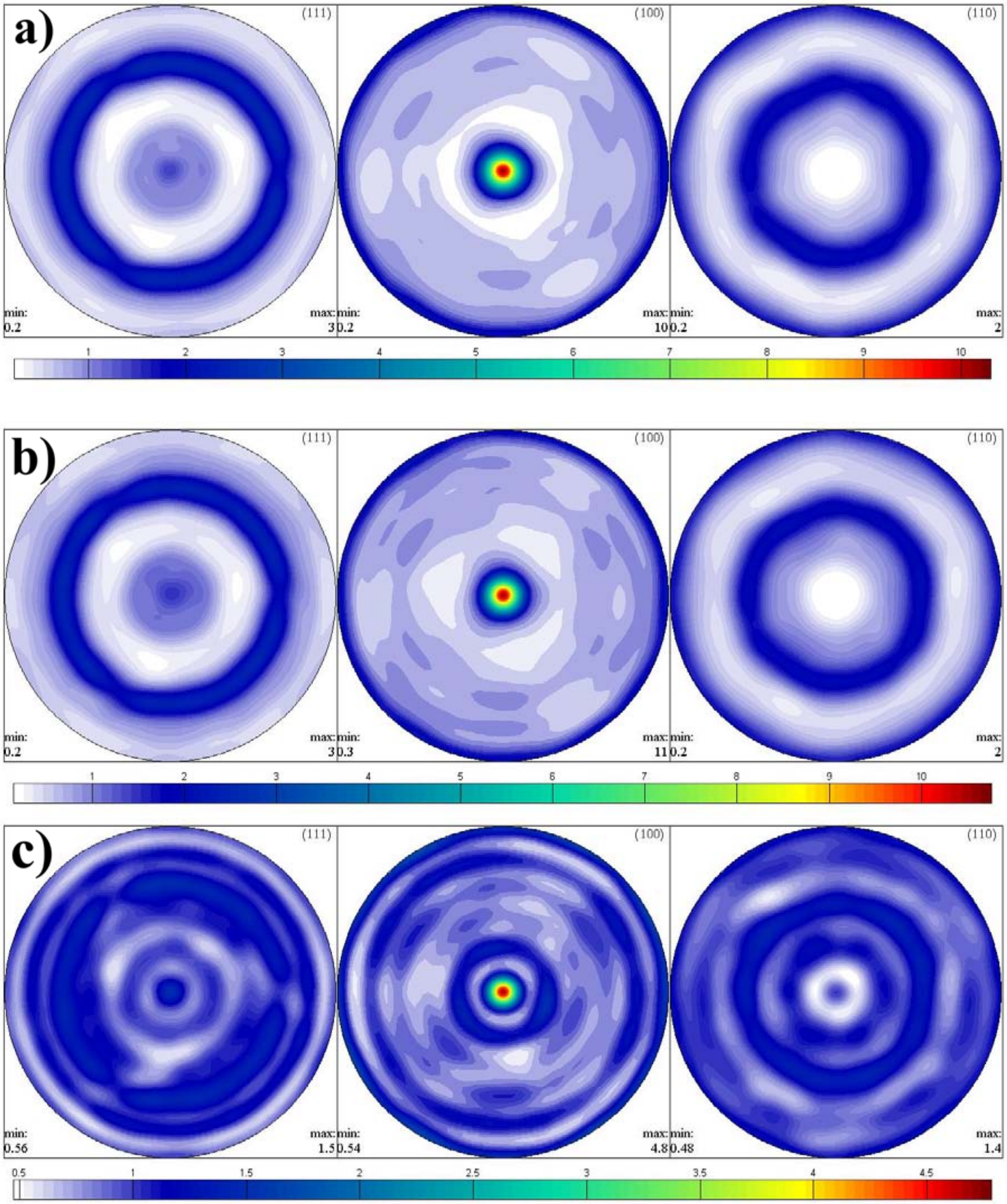
a)
(111)
(100)
(110)
min:
0.2
max:
3
min:
0.2
max:
10
min:
0.2
max:
2
1
2
3
4
5
6
7
8
9
10
b)
(111)
(100)
(110)
min:
0.2
max:
3
min:
0.3
max:
11
min:
0.2
max:
2
1
2
3
4
5
6
7
8
9
10
c)
(111)
(100)
(110)
min:
0.56
max:
1.5
min:
0.54
max:
4.8
min:
0.48
max:
1.4
0.5
1
1.5
2
2.5
3
3.5
4
4.5

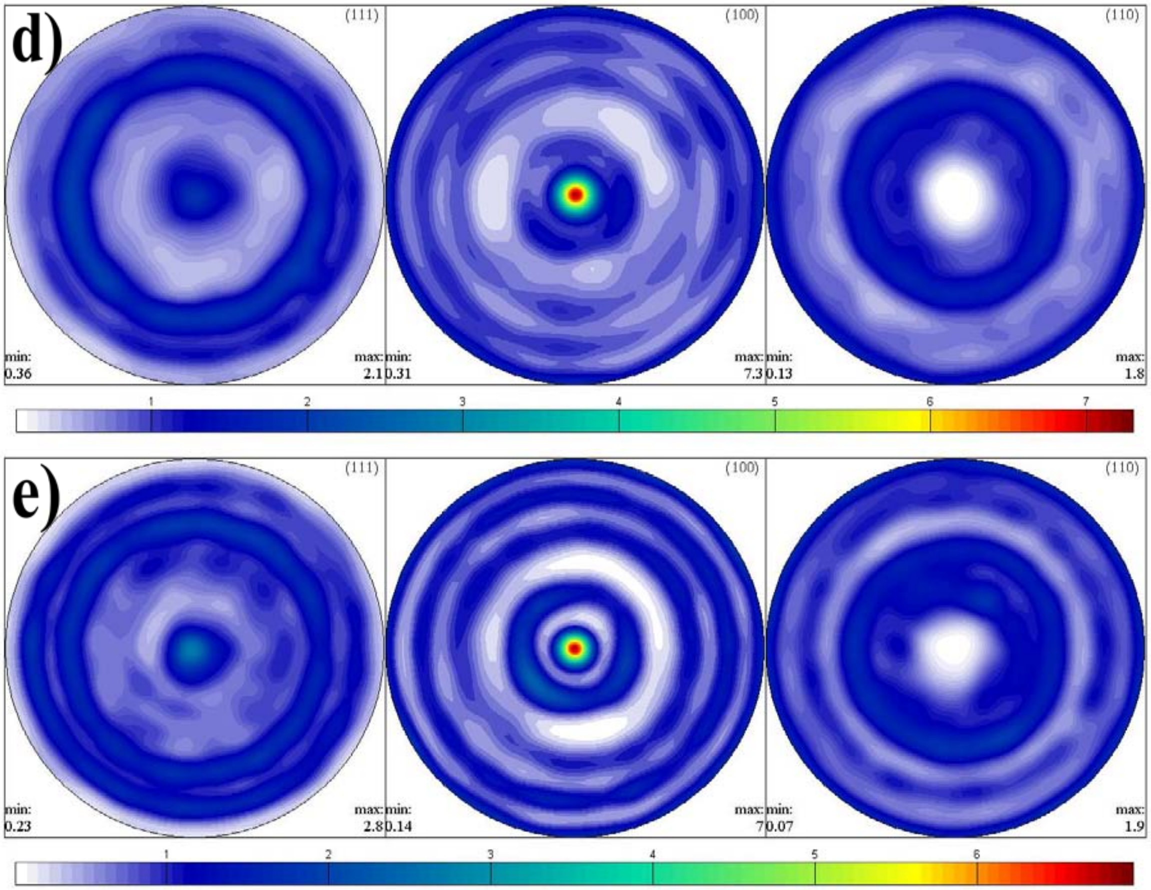

Figure 4.5 <111>, <100> and <110> recalculated Pole Figures for a) Ni-24.9at. % Fe alloy, b) Ni-33.1at. % Fe alloy, c) Ni-44.2at. % Fe alloy, d) Ni-54.2at. % Fe alloy, e) Ni-60.2at. % Fe alloy.

The volume fraction of the two fibre components of <100> and <111> are calculated by means of MATLAB-MTEX software. The spread angle is 10^{o} with ±1° error. As shown in Figure 4.6, the volume fraction of (100) is larger than that of (111) fibre. The Ni-44.2 at. % Fe alloy exhibits the lowest value of (100) volume fraction. A higher or a lower Fe content increases the volume fraction. The volume fraction values are listed in Table 4.1.

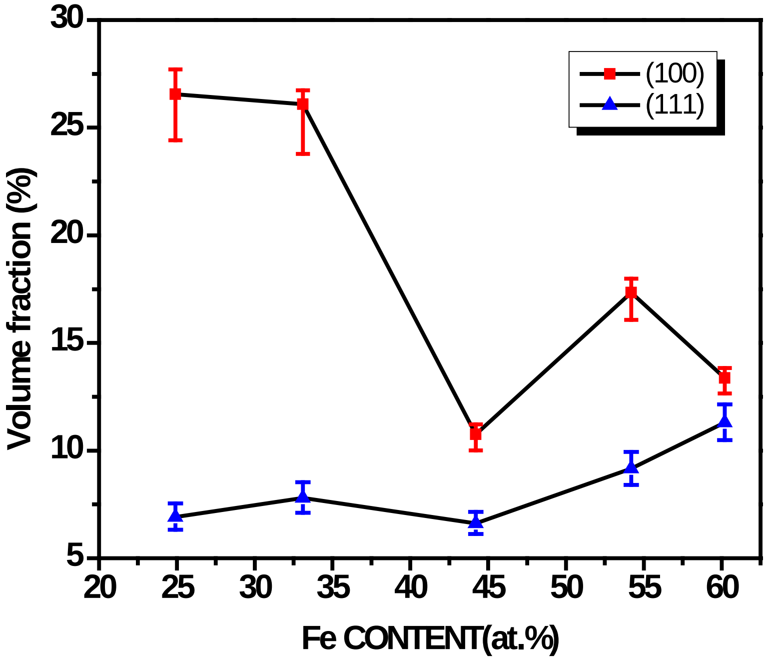

Figure 4.6 Volume fraction of (100) and (111) fibre texture components as a function of Fe content.

Table 4.1 Volume fraction of (100) and (111) fibre texture components.

Sample (at. %)	Volume fraction	
	(100)	(111)
24.9	26.56	6.92
33.1	26.09	7.8
44.2	10.76	6.62
54.2	17.34	9.16
60.2	13.37	11.3

4.2 Magnetic properties

The hysteresis loops were measured with a magnetic field parallel ($\varphi = 0°$) or perpendicular ($\varphi = 90°$)) to the sample plane at 298K and 2K. As shown in Figure 4.7, and 4.8, all the electrodeposited nanocrystalline Ni-Fe alloys with different Fe content exhibit narrow magnetization curves which indicates very low hysteresis losses

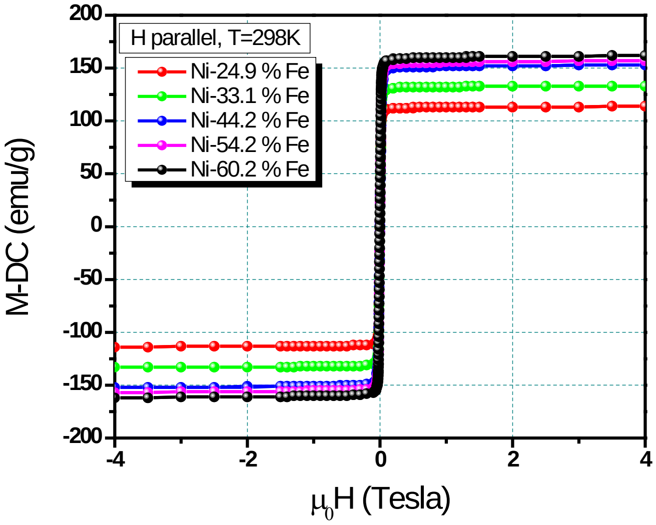

a) Hysteresis loops with magnetic field parallel to the samples plane at 298K.

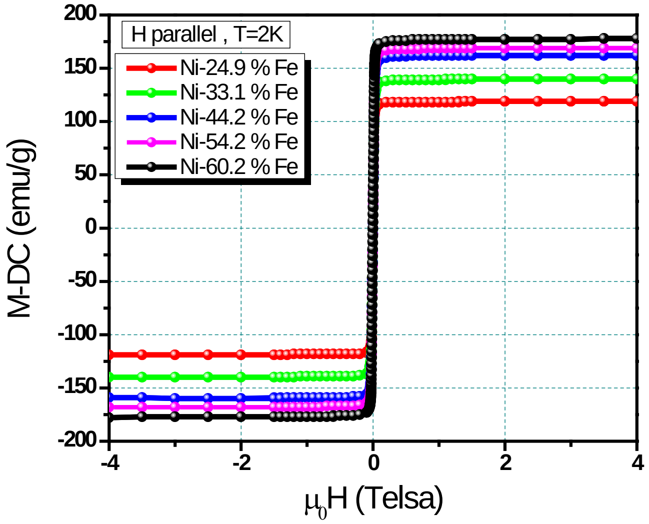

b) Hysteresis loops with magnetic field parallel to the samples plane at 2K.

Figure 4.7 Hysteresis loops for Ni-Fe alloys with different Fe content with magnetic field parallel to the sample plane at a) 298K and b) 2K.

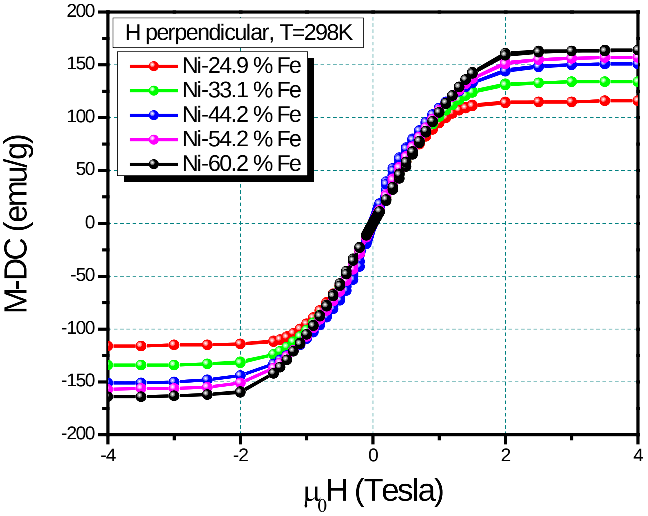

c) Hysteresis loops with magnetic field perpendicular to the samples plane at 298K.

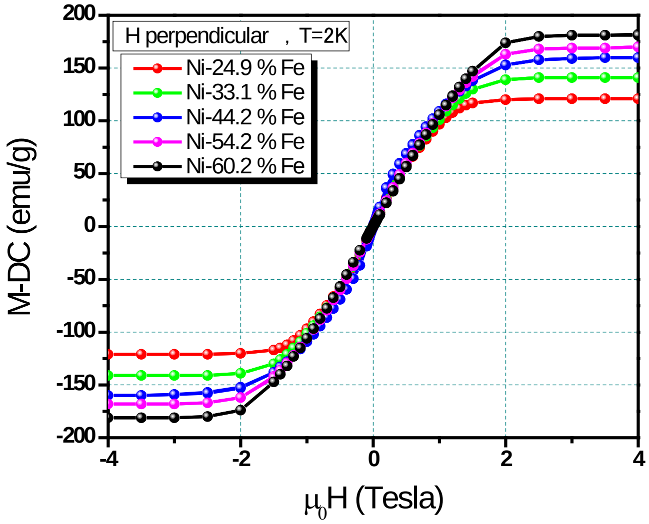

d) Hysteresis loops with magnetic field perpendicular to the samples plane at 2K.

Figure 4.8 Hysteresis loops for Ni-Fe alloys with different Fe content with magnetic field perpendicular to the sample plane at c) 298K and d) 2K.

The parallel field hysteresis loops clearly show that the magnetization approached saturation state under a small magnetic field of about 1000Oe. However, when the magnetic field is applied perpendicular to the samples plane, a large magnetic field is required to saturate the magnetization. This can be attributed to the large shape anisotropy for thin foil samples as shown in Figure 4.9. When the applied field is oriented parallel to the sample plane, the action of magnetic moments aligning with the field requires less energy and this results in easy and fast rotation of magnetic moments towards the applied field direction.

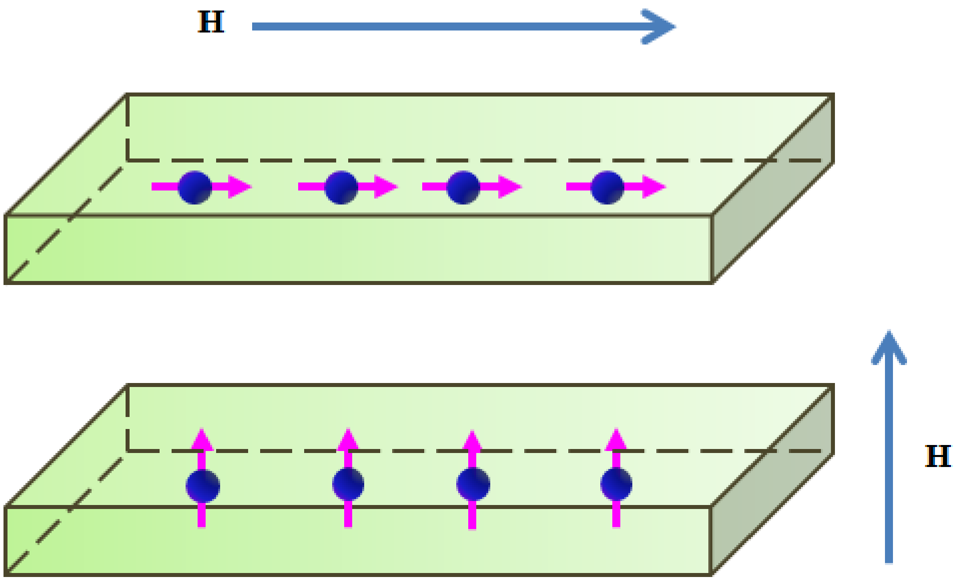

Figure 4.9 Two arrangements of parallel dipoles under external magnetic field: (a) stable, (b) unstable.

The saturation magnetization is plotted as a function of Fe content in Figure 4.10. The saturation magnetization increased linearly with increasing Fe content, which can be attributed to the increase of magnetic moment caused by larger Bohr magneton of Fe atoms as compared to Ni atoms. The number of Bohr magnetrons per atom is 2.6 and 0.6 for Fe and Ni. However, one observes no strong temperature-dependence of the magnetization in all Ni-Fe alloys. The magnetization at 2K is just slightly higher than at 298K, but with the increasing Fe content, the saturation magnetization difference becomes larger.

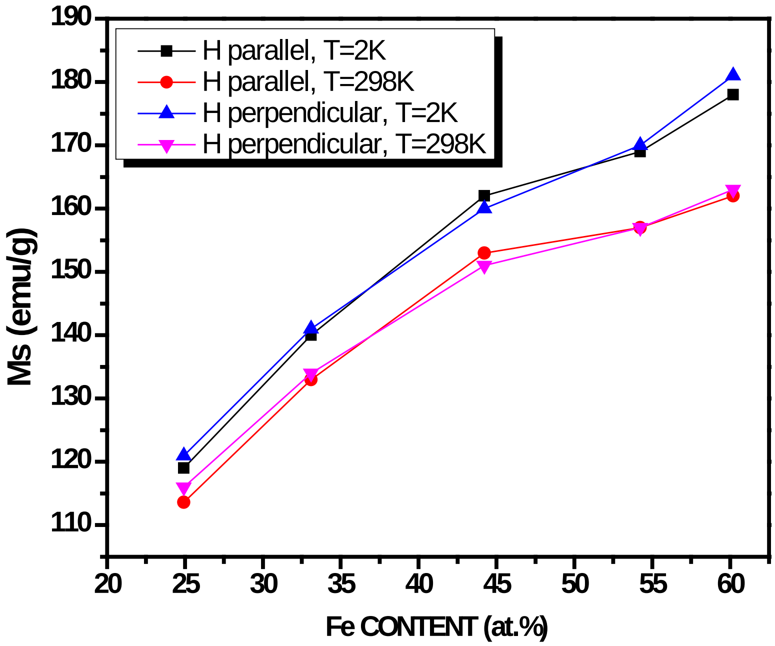

Figure 4.10 Saturation magnetization as a function of Fe content for nanocrystalline Ni-Fe alloys.

Coercivities of nanocrystalline Ni-Fe alloys were obtained from the hysteresis loops with the magnetic field applied parallel and perpendicular to the samples plane at 2K and 298K. The coercivity decreases with Fe content increasing in the Fe range from 24.9at. % to 44.2at. %, and then increases. As shown in Figure 4.11, the minimum value of 5.9Oe was observed for 44.2at. % Fe Ni-Fe alloy at 298K with the orientation of a magnetic field a perpendicular to the specimen surface.

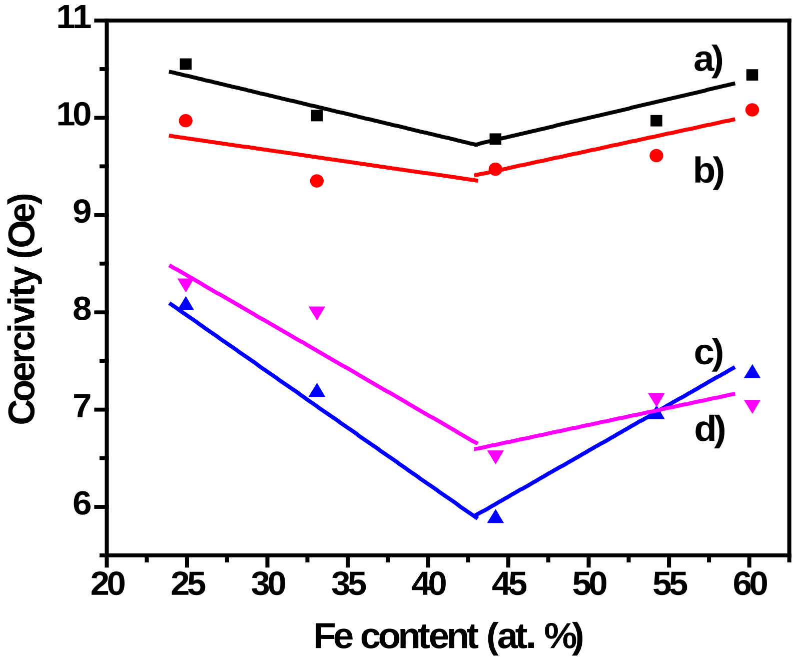

Figure 4.11 Variation of coercivity with Fe content with magnetic field a) parallel at 2K, b) parallel at 298K, c) perpendicular at 2K, d) perpendicular at 298K.

Figure 4.12 shows the coercivity of the nanocrystalline Ni-Fe alloys varied with the grain size. The cylinder (Green online) represents the range of our experiment results, which are in good agreement with the Random Anisotropy Model. According to the Random Anisotropy Model, when the average grain size (D) is larger than the ferromagnetic exchange length, $\mathrm{H_c} \sim 1/\mathrm{D}$, as D decreases to a value which equals to the ferromagnetic exchange length, $\mathrm{H_c}$ peaks. Then one observes a D^6 law dependence of the coercivity as D decreases further. In the present work, all the nanocrystalline Ni-Fe alloys are in the range of D^6 law as presented in Figure 4.12.

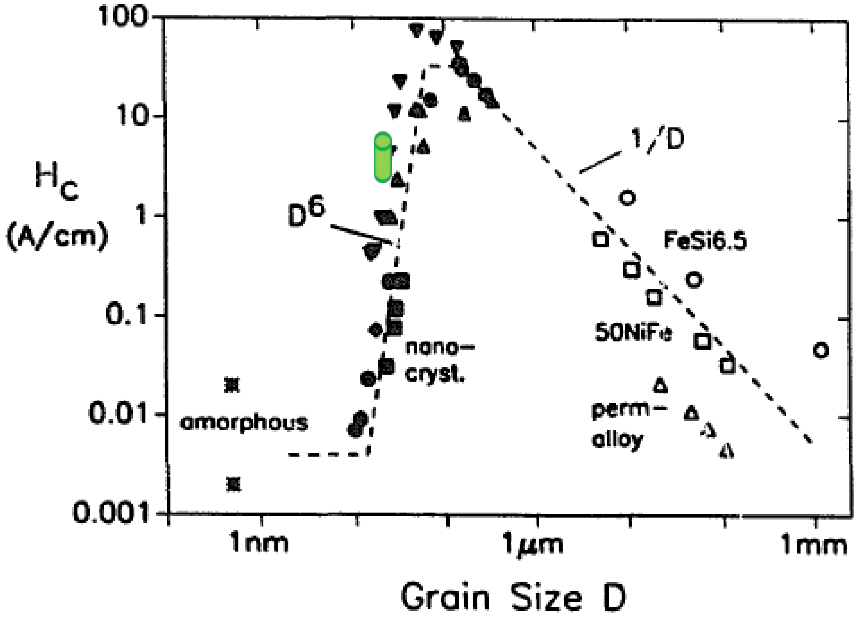

(▲) FeNbSiB,(●) FeCuNbSiB, (◆) FeCuVSiB, (■) FeZrB, (▼) FeCoZr

Figure 4.12 Coercivity as a function of a grain size for various soft magnetic metallic alloys [43]. (🟩) coercivity range of nanocrystalline Ni-Fe alloys studied in this work.

4.3 Effective Magneto-crystalline Anisotropy

The high magnetic field region of the magnetization process is determined by a variety of processes, such as, anisotropy, spin wave, susceptibility. An effective way to describe this process is the Law of Approach to Saturation (LATS), as discussed in Section 1.1.3.

According to the LATS, by fitting the high-field magnetization curve using equation (1.11) with least square method, a_2 values can be obtained for nanocrystalline Ni-Fe alloys with different Fe content, then the effective magneto-crystalline anisotropy can be calculated by equation (1.18).

In order to test whether or not the Law of Approach to Saturation is applicable for nanocrystalline Ni-Fe alloys, the magnetization M as a function of $\frac{1}{\sqrt{H}}$ and $\frac{1}{H^2}$ were plotted for all the samples with external magnetic field parallel to the sample plane. As shown in figure 4.13, the field dependence of $\frac{1}{\sqrt{H}}$-law was found with the applied field smaller than 400Oe, but as Fe content increases, this value decreased. As mentioned earlier, the $\frac{1}{\sqrt{H}}$ term is dominant in low field region and it is attributed to the lattice defects. It is clearly shown in figure 4.13 that the slope of the fitting line is higher as the Fe content increases. It indicates that the value of $a_1$increases with increasing ratio of Fe atoms to Ni. This is also confirmed by TEM observations which revealed that the amount of twining defects increased with Fe additions. However, when the applied field is larger than 400Oe, a relationship of $\frac{1}{H^2}$-law is observed for all Ni-Fe alloys as presented in Figure 4.14.

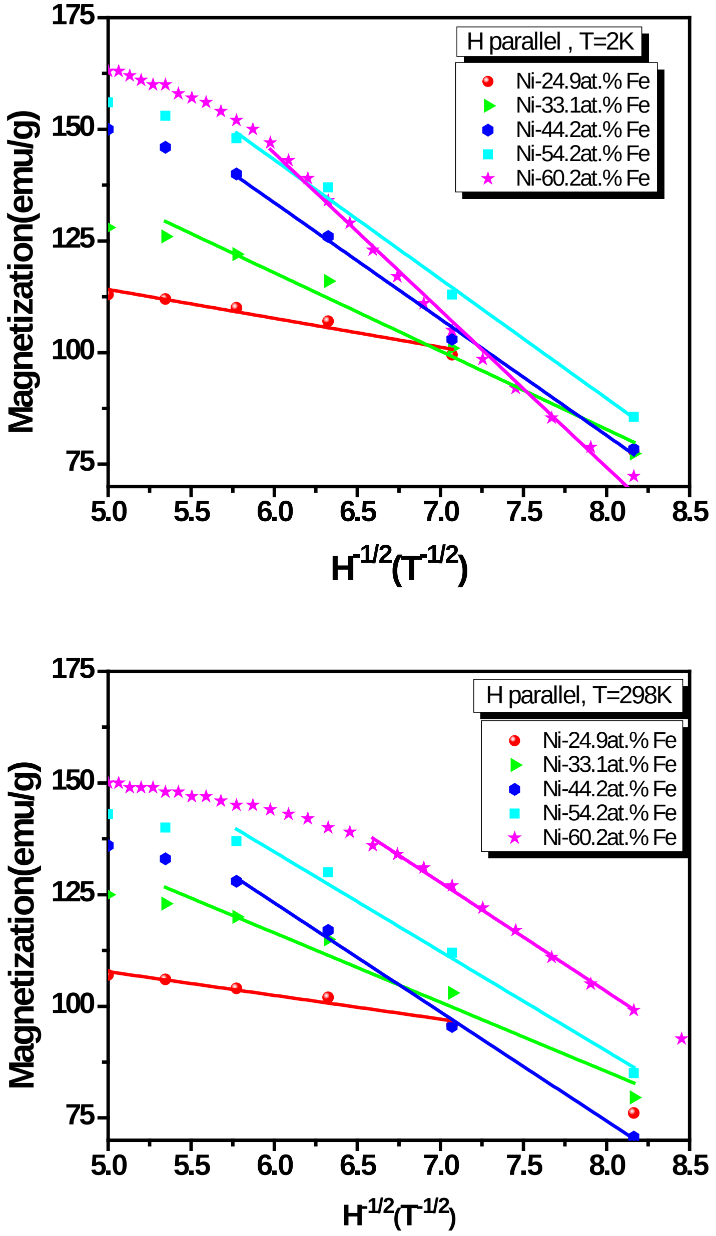

Figure 4.13 Magnetization as a function of $\frac{1}{\sqrt{H}}$ for nanocrystalline Ni-Fe alloys with different Fe content.

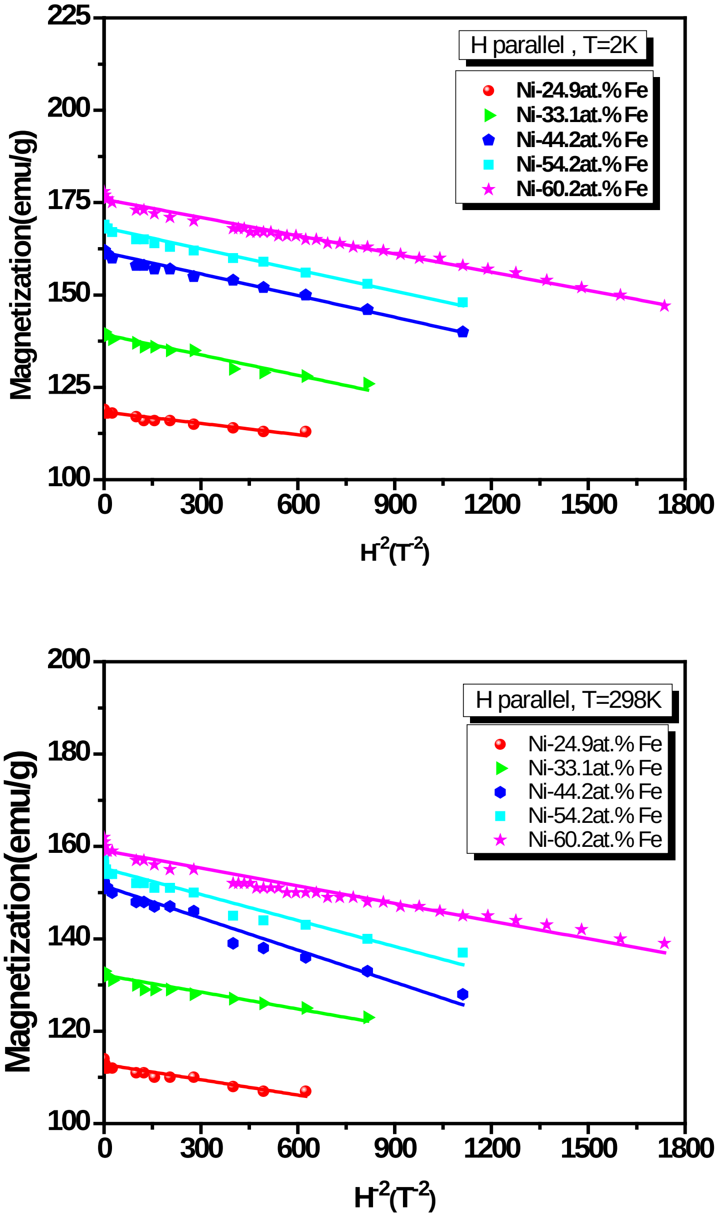

Figure 4.14 Magnetization as a function of $\frac{1}{H^2}$ for nanocrystalline Ni-Fe alloys with different Fe content.

The above results confirm that the law of approach to saturation can be used to analyse the magnetic properties of Ni-Fe alloys. As shown in figure 4.15, the open squares are the experimental data, and the solid lines are the best fitting according to the lease square method. The fitting parameters are listed in Table 4.2. The difference of the saturation magnetization between observed values from the magnetization curves and calculated values from fitting the experimental data is less than 3%, which indicates that the law of approach to saturation is suitable to the nanocrystalline Ni-Fe alloys. The effective magneto-crystalline anisotropy constants were calculated by substituting the a_2 values into equation (1.18). All the calculated values are also listed in Table 4.2.

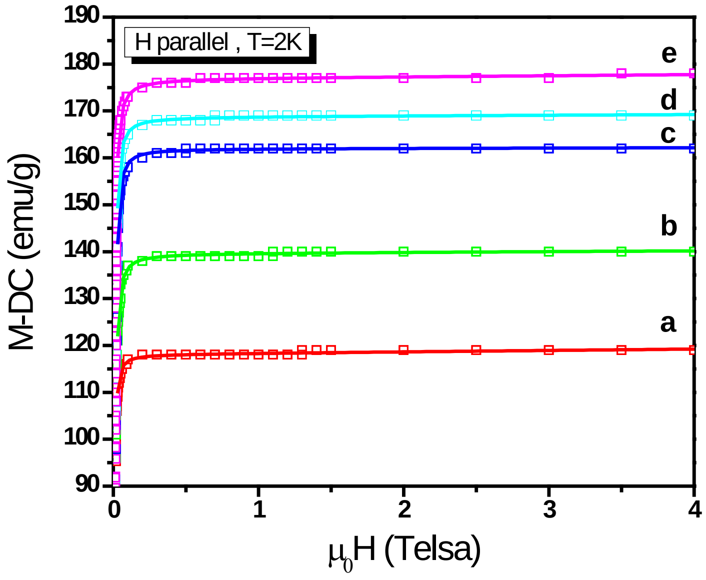

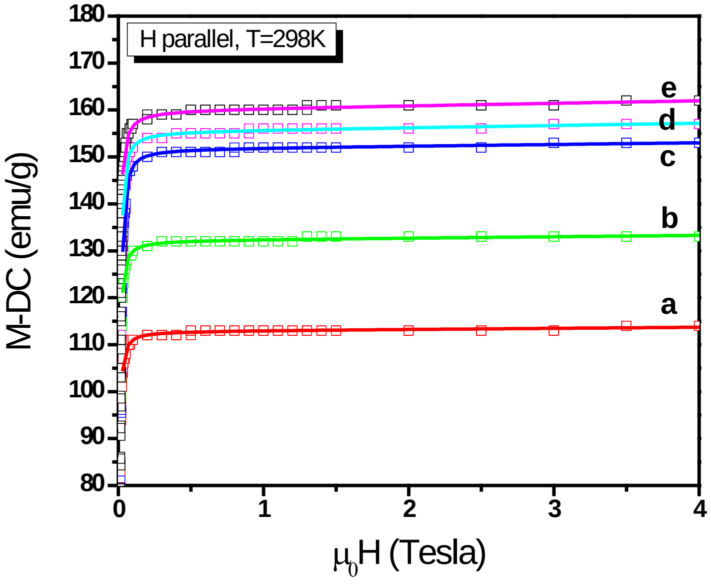

Figure 4.15 the open squares are the experimental data, the solid lines are the best fitting according to the least squares method for a) Ni-24.9at. % Fe alloy, b) Ni-33.1at. % Fe alloy, c) Ni-44.2at. % Fe alloy, d) Ni-54.2at. % Fe alloy, e) Ni-60.2at. % Fe alloy.

Table 4.2 The values of $\mathrm{M_s}$, $\mathrm{a_2}$ and $\mathrm{K_{eff}}$ obtained from fitting the magnetization curves.

Sample	T=2K			T=298K		
	M_s (emu/g)	a_2 $(10^4\mathrm{Oe})^2$ x 10^{-5}	K_{eff} (erg/cc) x 10^5	M_s (emu/g)	a_2 $(10^4\mathrm{Oe})^2$ x 10^{-5}	K_{eff} (erg/cc) x 10^5
Ni-24.9at.%Fe	118.11	3.32	1.12	112.87	2.29	0.89
Ni-33.1at.%Fe	139.65	6.10	1.57	132.23	3.06	1.06
Ni-44.2at.%Fe	161.99	7.46	1.78	151.74	7.72	1.71
Ni-54.2at.%Fe	168.79	5.97	1.77	155.42	5.33	1.56
Ni-60.2at.%Fe	176.98	3.44	1.72	160.01	1.83	1.14

The effective magneto-crystalline anisotropy is plotted as a function of Fe content in Ni-Fe nanocrystalline alloys in Figure 4.16. At first the value of K_{eff} increases as Fe content increases, reaches a maximum value for 44.2at. %Fe sample, and then it drops down. The results clearly show reduction in K_{eff} value with increasing temperature from 2K to 298K. This is consistent with the previous studies that the values of effective magneto-crystalline anisotropy decreases with increasing temperatures and reaches very low values around the Curie temperature [44].

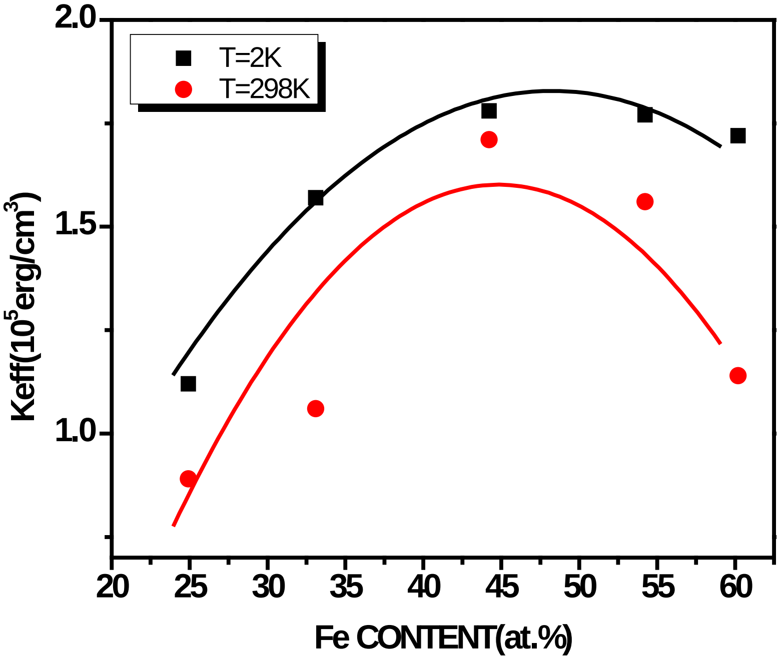

Figure 4.16 The effective anisotropy as a function of Fe content for Ni-Fe alloys at 2K and 298K.

4.4 Exchange stiffness constant and exchange length

The values of the magnetic exchange stiffness constant A can be determined from the temperature dependence of the saturation magnetization. According to the Bloch $T^{3/2}$ law, the ratio of the saturation magnetization is given by

$$\frac{M_s(T)}{M_s(0)} = 1 - BT^{3/2} \tag{4.1}$$

The parameter is related to the exchange stiffness by the following relation:

$$B = 0.0587(Qs)^{\frac{1}{2}}\left(\frac{k_B}{2Aa}\right)^{3/2} \tag{4.2}$$

Where Q is the number of lattice points per unit cell, for simple cubic, BCC and FCC lattice, Q equals to1, 2 and 4, respectively. k_B is Boltzmann's constant, a is the lattice parameters calculated from the XRD results. s is called the spin quantum number which is given by

$$s = \frac{M_s(0)a^3}{Qg\mu_B} \tag{4.3}$$

Where μ_B is the Bohr magneton. g is the spectroscopic g factor ($g = 2.002290716(10)$). The exchange stiffness is a temperature dependent parameter and can be related to the spin wave stiffness constant D by the following relation:

$$A(T) = \frac{M_s(0)D}{2g\mu_B}\left(\frac{M_s(T)}{M_s(0)}\right)^2 \quad (4.4)$$

Substituted into equation 4.5,

$$B = 0.0587\,\frac{g\mu_B}{M_s(0)}\left(\frac{k_B}{D}\right)^{3/2} \quad (4.5)$$

From the hysteresis loops, the saturation magnetization M_s can be obtained at each temperature. As shown in Figure 4.17, the $M_s(T)/M_s(0)$ is plotted versus $T^{3/2}$. These experimental data have been fitted linearly.

From the slopes of $M_s(T)/M_s(0)$ vs $T^{3/2}$, the spin wave stiffness constants D were calculated and are listed in Table 4.3. For all the nanocrystalline Ni-Fe alloy samples, the D values are the same order of magnitude as these reported in references and are increased with increasing Fe content. The exchange stiffness constant can be calculated by using Equation 4.4. The values are listed in Table 4.3. The result shows a good agreement with previous data A $=1.1\times10^{-6}$ erg/cc (45), and A = $(1.00\pm0.20)\times10^{-6}$ erg/cc (46). In addition, the exchange stiffness constant A slightly decreased as increasing temperature from 2K to 298K.

According to the random anisotropy model, by knowing the value of effective magneto-crystalline anisotropy K_{eff} and the exchange stiffness A, the exchange length can be calculated using the equation

$$L_{ex} = \varphi_0 \sqrt{\frac{A}{K_{eff}}} \tag{4.6}$$

Where φ_0 is equal to 1. The values of L_{ex} are also listed in Table 4.3. As shown in Table 4.3, the exchange length decreases as Fe content increases.

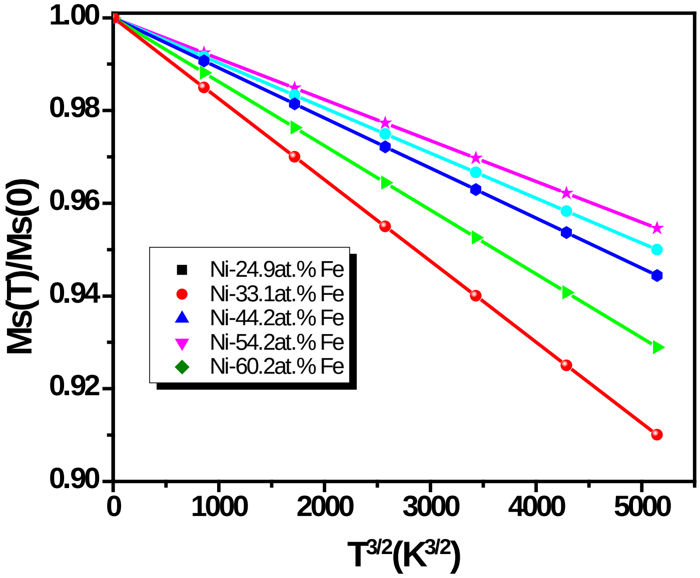

Figure 4.17 Temperature dependence of the saturation magnetization plotted versus $T^{3/2}$ for Ni-Fe nanocrystalline alloys with different Fe content.

Table 4.3 Calculated exchange stiffness and exchange length values.

samples	Spin wave stiffness constant D (meVÅ)	Exchange stiffness A (erg/cm) x 10^{-6}		Exchange length L_{ex} (nm)	
		T=2K	T=298K	T=2K	T=298K
Ni-24.9at.%Fe	322.54	0.75	0.68	26	28
Ni-33.1at.%Fe	295.85	0.71	0.64	21	25
Ni-44.2at.%Fe	1263.95	0.67	0.59	19	19
Ni-54.2at.%Fe	214.78	0.59	0.51	18	18
Ni-60.2at.%Fe	155.89	0.55	0.45	17	19

4.5 Correlation between K_{eff}, H_c, μ and L_{ex}

As discussed before, one of the most important predictions of the Random Anisotropy Model is that the coercivity can be related to the power of six of the grain size (i.e. Hc~D^6).

$$H_c = P_c \frac{K_{eff}}{M_s} = P_c \frac{K_1}{M_s} \left(\frac{D}{L_{ex}}\right)^{3/2} = P_c \frac{K_1^4 D^6}{M_s A^3} \quad (4.7)$$

To investigate the accuracy of the above relationship, the experimental values of saturation magnetization, coercivity and the obtained effective magneto-crystalline anisotropy from law of approach to saturation are compared against each other and are listed in Table 4.4. Using the equation 4.7, P_c values for different Fe content samples were deduced, the values are comparable to the previous reported simulation values by Alben [47]. Ref [47] gives that the Pc is around 0.05 for perfectly random amorphous materials. In our calculation, the range of Pc is between 0.03 and 0.06. This is a good proof that the random anisotropy model is suitable to predict magnetic properties of electrodeposited nanocrystalline Ni-Fe alloys studied here.

Table 4.4 The values of saturation magnetization, effective magneto-crystalline anisotropy, coercivity and Pc.

	M_s (emu/cm^3)		K_{eff} (erg/cc) x 10^5		H_c (Oe)		P_c	
	T=2K	T=298K	T=2K	T=298K	T=2K	T=298K	T=2K	T=298K
Ni-24.9at.%Fe	538.72	514.28	1.12	1.57	10.89	10.40	0.05	0.06
Ni-33.1at.%Fe	556.55	528.72	1.78	1.77	10.375	9.79	0.04	0.05
Ni-44.2at.%Fe	567.23	535.72	1.72	0.89	10.09	9.89	0.03	0.03
Ni-54.2at.%Fe	633.58	588.59	1.06	1.71	10.335	9.95	0.04	0.04
Ni-60.2at.%Fe	809.42	736.66	1.56	1.14	11.01	10.80	0.05	0.06

4.6 Effect of Fe in nanocrystalline Ni-Fe alloys

(I) The first effect of Fe in nanocrystalline Ni-Fe alloys is that saturation magnetization increases with increasing Fe content. As shown in Figure 4.18, the saturation magnetization for pure Ni and Fe are 58.57emu/g and 221.71 emu/g from literature [48], respectively. The reason for the increasing of the saturation magnetization can be attributed to the larger Bohr magnetrons of Fe (=2.6 per atom) as compared to Ni atoms (0.6 per atom).

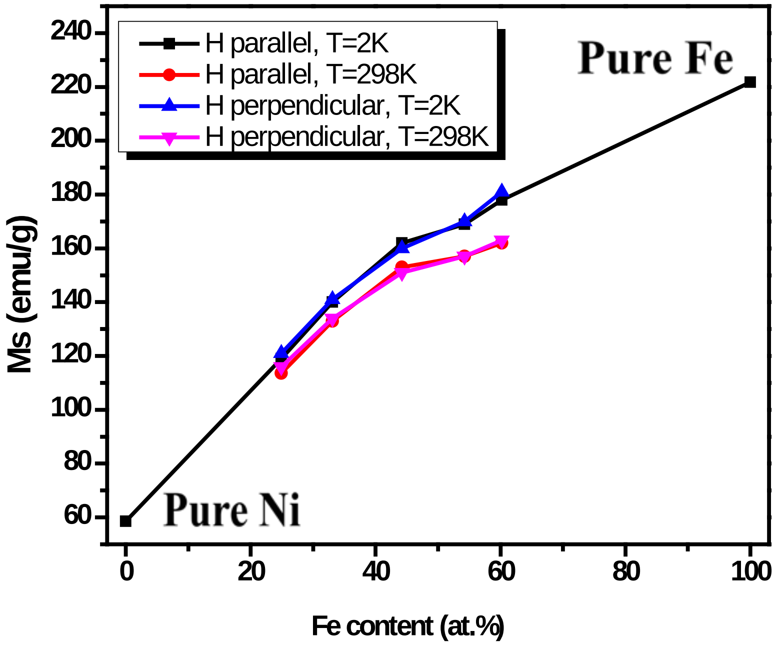

Figure 4.18 Saturation magnetization as a function of Fe content for nanocrystalline Ni-Fe alloys, pure Ni and pure Fe [48].

(II) The second effect is that the ferromagnetic exchange length decreases with increasing Fe content as shown in Figure 4.19. The influence of exchange interactions between grains are weakened by introducing Fe to Ni.

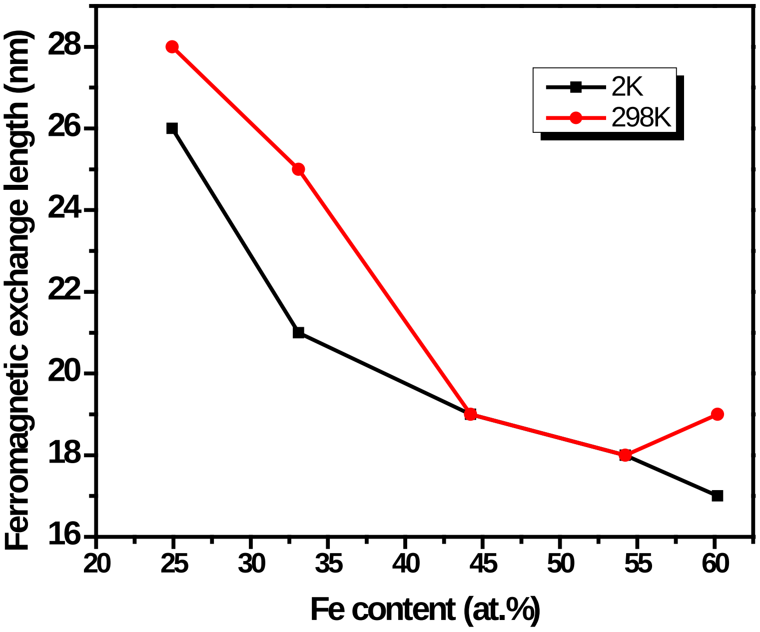

Figure 4.19 Ferromagnetic exchange length as a function of Fe content.

4.7 Inverted hysteresis loops

Hysteresis loop behaviour is important phenomena observed in a range of materials under the application of external magnetic field. The regular hysteresis loops have common character, when the field decreases from the positive saturation field to zero, the magnetization does not decrease to zero but remains positive, producing characteristic hysteresis. However, an inverted hysteresis loop means that the hysteresis loop progress in a clockwise direction with negative remanence i.e., $M_r < 0$. The difference between regular hysteresis loop and inverted hysteresis loop is shown in Figure 4.20.

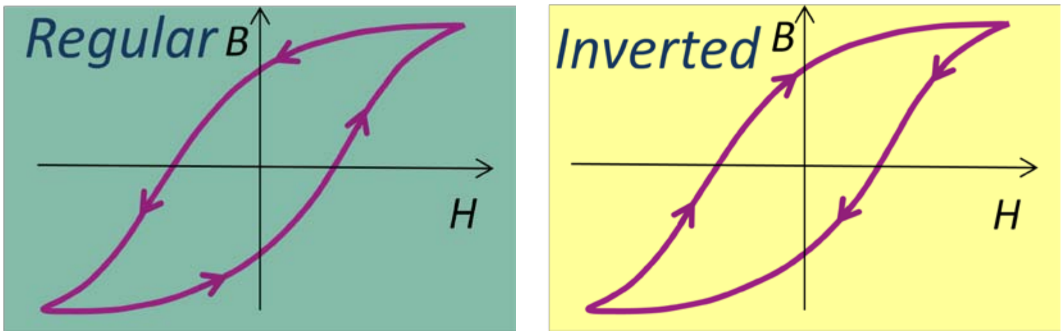

Figure 4.20 Schematic diagram showing the difference between regular hysteresis loop and inverted hysteresis loop.

The inverted hysteresis loop with negative remanence was observed in amorphous Gd-Co films in 1970s [49]. This phenomenon also has been observed in some exchange-coupled multilayers [50-56]. It can be interpreted either by interface interaction based on antiferromagnetic interlayer exchange or based on the demagnetizing effect [57-58].

In the present work, all the electrodeposited nanocrystalline Ni-Fe alloy samples with different Fe content exhibited inverted hysteresis loops, with applied magnetic field both parallel and perpendicular to the samples plane at 2K and 298K, as shown in Figure 4.21. The remanences are negative for Ni-Fe alloys with different Fe content as shown in Figure 4.22.

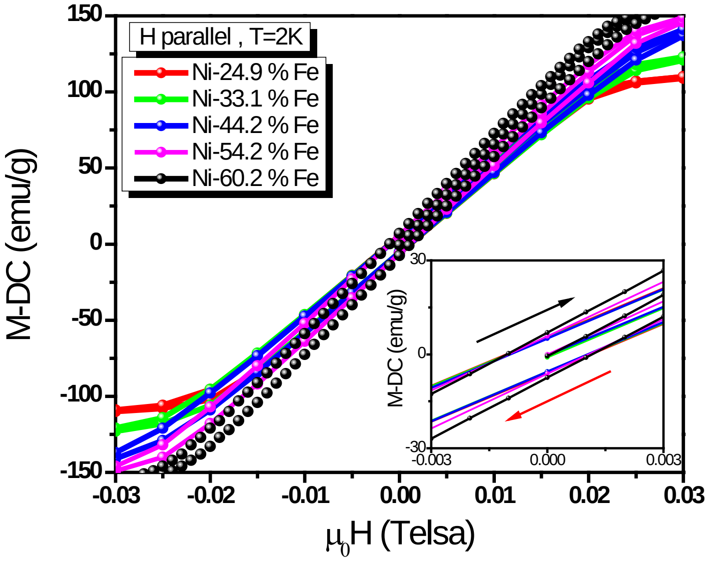
H parallel , T=2K
Ni-24.9 % Fe
Ni-33.1 % Fe
Ni-44.2 % Fe
Ni-54.2 % Fe
Ni-60.2 % Fe
M-DC (emu/g)
150
100
50
0
-50
-100
-150
-0.03
-0.02
-0.01
0.00
0.01
0.02
0.03
μ_0H (Telsa)
30
0
-30
-0.003
0.000
0.003

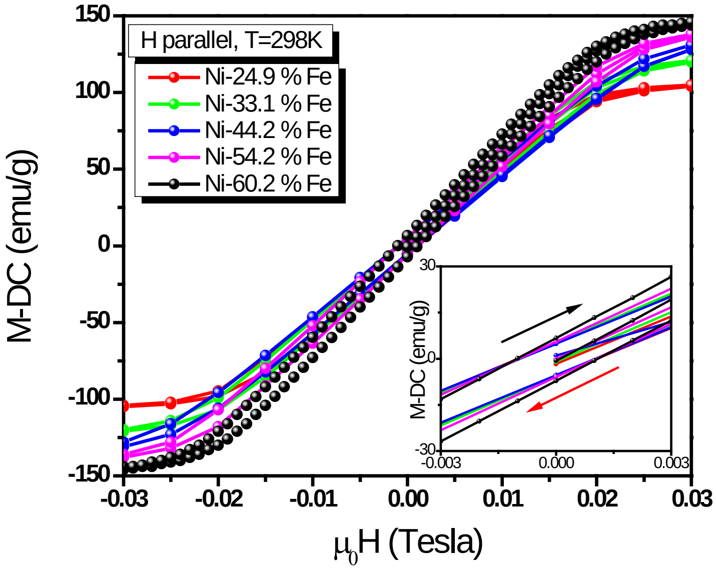
H parallel, T=298K
Ni-24.9 % Fe
Ni-33.1 % Fe
Ni-44.2 % Fe
Ni-54.2 % Fe
Ni-60.2 % Fe
M-DC (emu/g)
150
100
50
0
-50
-100
-150
-0.03
-0.02
-0.01
0.00
0.01
0.02
0.03
μ_0H (Tesla)
30
0
-30
-0.003
0.000
0.003

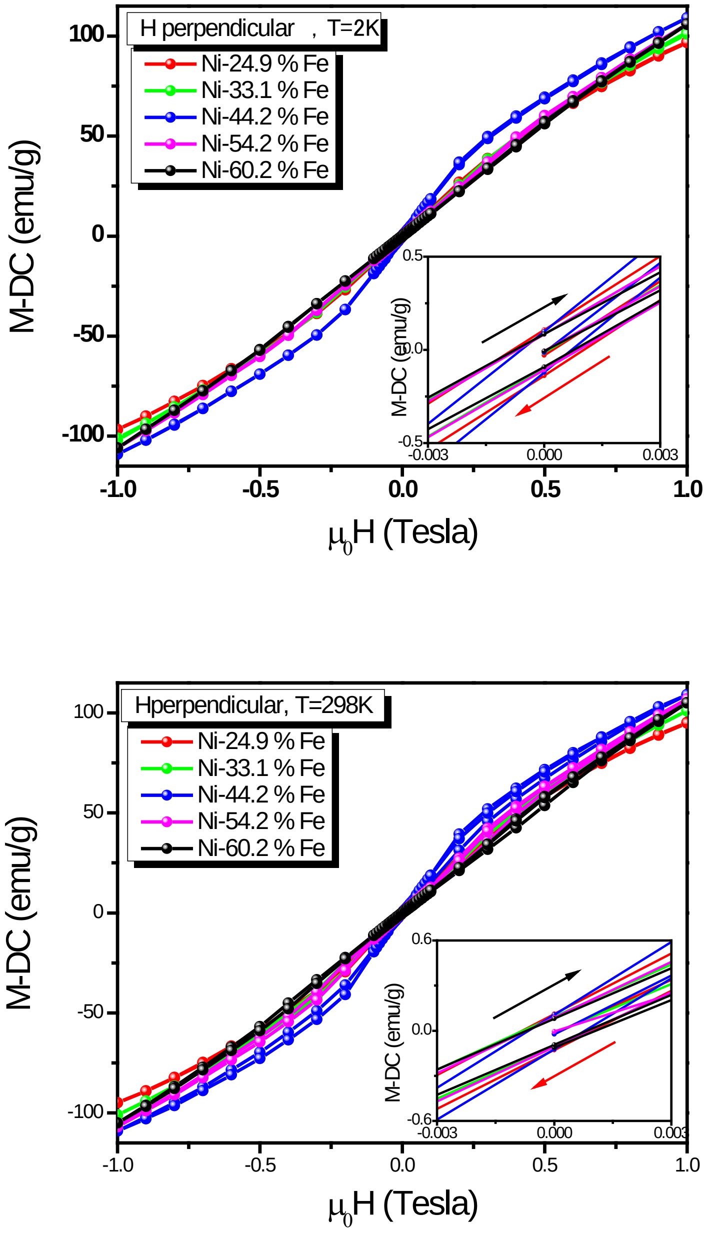

Figure 4.21 Inverted parallel and perpendicular hysteresis loops of nanocrystalline Ni-Fe alloys with different Fe content. Insets are enlarged view of the same curves.

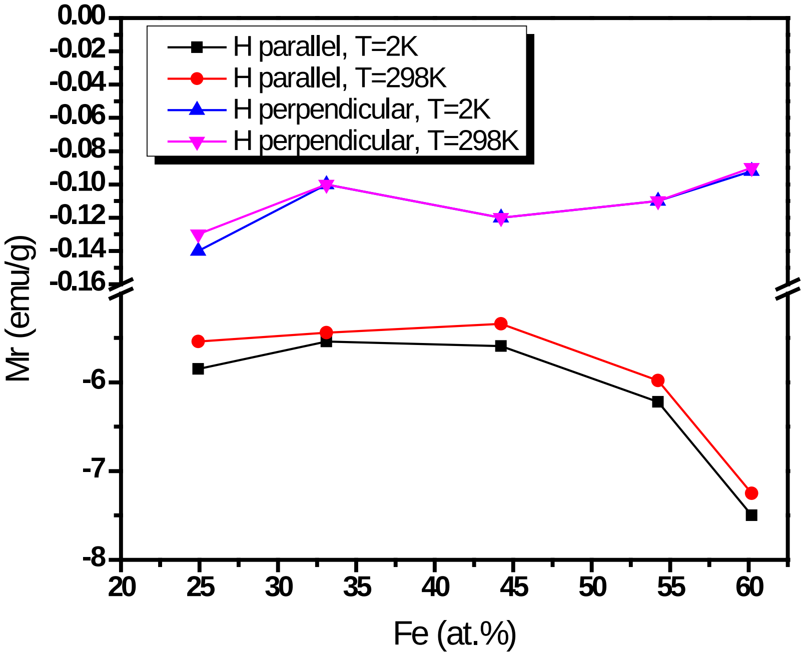

Figure 4.22 In plane and out of plane remanence as a function of Fe content at 2K and 298K.

There are three possibilities of the origin of the inverted hysteresis loops phenomenon for of electrodeposited nanocrystalline Ni-Fe alloys:

(I) Inappropriate or asymmetric sample positioning could result in a negative net area of hysteresis loops [59]. Figure 4.23 presents typical arrangements of SQUID magnetometer in the magnetic field spaces along with the coordinates. The magnetic field is along the x-axis and the coils are normal to the axis. The first step of a typical SQUID experimental procedure is sending sample into the chamber of SQUID magnetometer and make sure the sample located at the origin (x0=0,z0=0). Then the SQUID system will adjust the sample's position to the exactly correct place. However, if the location error is large enough, the inverted hysteresis loops would be obtained.

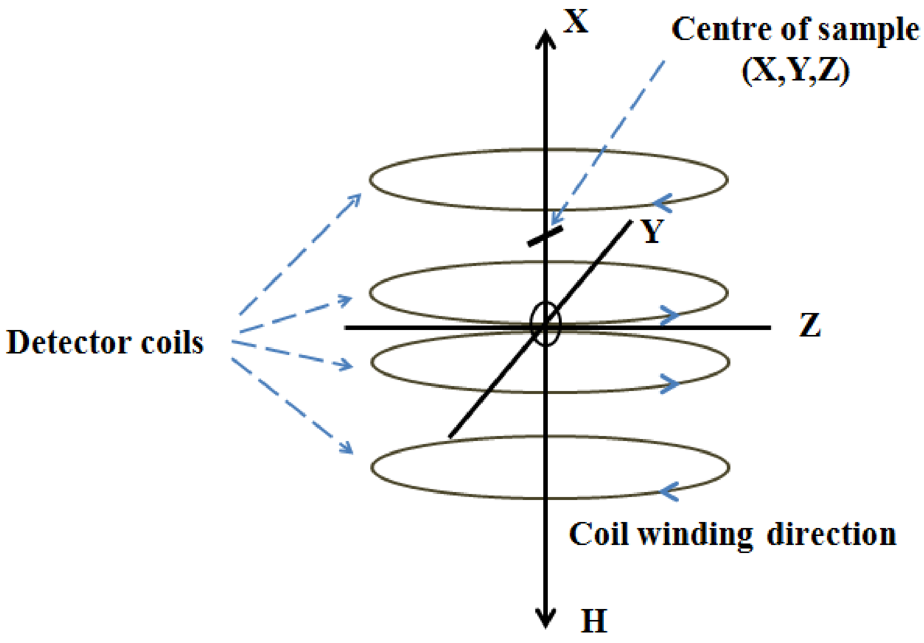

Figure 4.23 The sample arrangement in the field space of SQIUD magnetometer. The coordinates and notations are shown in the graph. The pickup coils in each figure are connected in series [59].

(II) Thin oxides layers on the samples surface could contribute to a negative remanence. The main reflection peaks of XRD patterns for all the nanocrystalline samples with a thin NiFeO layer are similar to those of the pure FCC Ni-Fe phase, except that the peaks are broader. One can infer from XRD study discussed in section 4.1 that the concentration of NiFeO on the surface should be less than a few percent. This is quite similar to the results reported before. The interactions between the surface oxides layers and the crystalline Ni-

Fe inside would block the domain rotation along the magnetic field after positive saturation magnetization state, and therefore the inverted hysteresis loops could arise for all the nanocrystalline Ni-Fe alloy samples.

(III) The interactions between the amorphous state in the grain boundaries and the crystalline state could be another reason resulting in the inverted hysteresis loops. However, based on the experiments carried out so far neither explanation is fully acceptable. A future work is needed to understand reasons behind inverted hysteresis behaviour in nanocrystalline Ni-Fe alloys studied here.

Chapter 5 Conclusions and Future work

This research has been devoted to the study of the magnetic properties of electrodeposited nanocrystalline Ni-Fe alloys with different Fe content from 24.9 at. % to 60.2 at. %. The research objectives proposed in Chapter 1 have been achieved, and the key findings and major contributions of this work are as follows:

1. The structure of nanocrystalline Ni-Fe alloys has been studied by the 2D-XRD analysis. The lattice parameter increases as the Fe content increases till 54.2 at. %, and then decreases due to the presence of the BCC phase.
2. Texture analysis reveals that all the electrodeposited samples develop fibre texture with strong <100> component and some contribution of the <111> component.
3. Magnetic measurements of nanocrystalline Ni-Fe alloys show that all the samples exhibit narrow hysteresis loops and soft magnetic behaviour. The saturation magnetization increases with increasing Fe content and also with decreasing temperature.

4. The magnetocrystalline anisotropy results show that the highest value of K_{eff} is obtained for 44.2 at. % Fe samples. The ferromagnetic exchange length decreases with increasing Fe content.
5. Since the ferromagnetic exchange length is larger than the grain size, the Random Anisotropy Model is suitable to describe properties of nanocrystalline Ni-Fe alloys.

Suggestions for future research:

1. We have shown the calculated magnetocrystalline anisotropy and coercivity, however, these results cannot be totally explained by Random Anisotropy Model which predicts that the coercivity should be increasing with increasing K_{eff}. In this work, the effective magnetocrystalline anisotropy reached the maximum for 44.2 at. % Fe sample, but this sample exhibits the lowest coercivity. Annealing experiments are recommended for all the nanocrystalline Ni-Fe samples to confirm the relationship between the grain size and coercivity.
2. According to the literature [59], the structure of grain boundaries can be attributed to the saturation magnetization and therefore may affect the magnetic properties.

Modelling efforts are needed to complete the analysis of the structure of grain boundaries and their effect on magnetic properties.

3. The reason of the inverted hysteresis loop phenomenon is still not clear. Magnetic measurements with polished samples are recommended to confirm if oxide layer on sample's surface can contribute to the appearance of the inverted hysteresis loop behaviour.
4. For detailed understanding of exchange interactions between individual grains and grain boundaries and to understand the role of texture in magnetic properties, simulations of the magnetic properties based on the Stoner-Wohlfarth theory are needed.

References

[1] J.Stöhr, H. C. Siegmann, Magnetism From Fundamentals to Nanoscale Dynamics, P4.

[2] http://www.nipic.com/show/1/24/4926479k15438cdd.html

[3] K.H.J. Buschow, F. R. de Boer, Physics of Magnetism and Magnetic Materials, P24.

[4] http://en.wikipedia.org/wiki/Magnetic_domain

[5] http://en.wikipedia.org/wiki/Saturation_(magnetic)

[6] B. D. Cullity, in Introduction to Magnetic Materials (Addison-Wesley, New York, 1972)

[7] http://en.wikipedia.org/wiki/Coercivity

[8] http://en.wikipedia.org/wiki/Remanence

[9] http://gravmag.ou.edu/mag_rock/mag_rock.html

[10] http://en.wikipedia.org/wiki/Magnetocrystalline_anisotropy

[11] H. Kronm¨uller, IEEE Trans. Magn. MAG-15, 1218(1979).

[12] W.F. Brown Jr., Phys. Rev. 58 (1940) 736.

[13] W.F. Brown Jr., Phys. Rev. 60 (1941) 139.

[14] L. Néel, J. Phys. Radium 9 (1948) 184

[15] Chikazumi S 1964 Physics of Magnetism (New York: Wiley) p 277

[16] Senoy Thomas, S H Al-Harthi, D Sakthikumar, I A-Omari, R V Ramanujan, Yasuhiko Yoshida and M R Anantharaman, J. Phys. D: Appl. Phys. 41, 155009(8pp), (2008)

[17] Z-Q. Jin, W. Tang, J.-R. Zhang, H.-X. Qin2, and Y.-W. Du, Eur. Phys. J. B 3,41-44 (1998)

[18] Oleg Heczko, Pekka Ruuskanen, Ludek Kraus, Vladimir Haslar, IEEE TRANSACTIONS ON MAGNETICS, Vol. 30, No. 20, 513-515 (1994)

[19] Kai Yuan ho, Xiang-Yuan xiong, Jiang Zhi, and Li-Zhi Cheng, J. Appl. Phys. Vol 74, Num.11, 6788-6790(1993)

[20] R. Alben, J. J. Becher, and M. C. Chi, J. Appl. Phys, 49,1653 (1978)

[21] G. Herzer, IEEE Trans. Magn. 25, 3327 (1989)

[22] H. Q. Guo, T. Reininger, H. Kronmuller, M. Rapp, and V. K. Skumrev, Phys. Status Solidi A 127, 519 (1991)

[23] M. Muller and N. Mattern, J. Magn. Magn. Mater. 136, 79 (1994)

[24] G.Herzer, Journal of Magnetism and Magnetic Materials 157/158, 133-136 (1996)

[25] R.Birringer, Materials Science and Engineering, A117 (1989) 33-43

[26] Gleiter, H., Pro.Matter.Sci., 33:224(1989)

[27] Yao,Y.D., Chen, Y. Y., Hsu, C.M., Lin,H.M., Tung, C.Y., Tai, M.F., Wang, D.H., Wu, K/ T., and Suo, C.T., Nanostruct. Mater., 6: 933(1995)

[28] Krill,C.E.,Merzoug, F., Krauss, W., and Birringer, R., Nanostruct. Mater., 9:455(1997)

[29] Aus, M.J., Szpunar, B., El-Sherik, A. M., Erb, U., Palumbo, G., and Aust, K.T., Scripta Metall. Mater., 27:1639 (1992)

[30] A. Robertson, U. Erb and G. Palumbo, NanoStructured Materials, Vol. 12, pp. 1035-1040,1999

[31] G. Palumbo, J. L. McCrea, U. Erb, Encyclopedia of nanoscience and Nanotechnology, Volume 1; pages 89-99 (2004)

[32] J. L. McCrea, G. Palumbo, G. D. Hibbard and U. Erb, Rev. Adv. Mater. Sci. 5, 252-258 (2003)

[33] H. Q. Li, F. Ebrahimi, Acta Materialia 51, 3905-3913 (2003)

[34] Wang S X, Sun N X, Yamaguchi M and Yabukami S 2000 Nature 407, 150

[35] Yong L and Arokia N 1997 Appl. Phys. Lett. 70, 526

[36] Hasegawa R 2004 Mater. Sci. Eng. A 375, 90

[37] Aravinda CL, Mayanna SM. Potentiostatic deposition of thon films of Ni-Fe alloys. Trans IMF 1999;77:87–8.

[38] http://en.wikipedia.org/wiki/Shape_factor_(X-ray_diffraction)

[39] http://www.tristantech.com/technotes_intro.html

[40] E.J. Swartzendruber, V.P. Itkin, and C.B. Alcock, ASM Handbook, Vol. 3, 1992

[41] Hongqi Li, Fereshteh Ebrahimi, Materials Science and Engineering A 347, 93-101 (2003)

[42] T. Osaka, M. Takai, Y. Sogawa, T.Momma, K. Ohashi, M. Saito, K. Yamada, J. Electrochem. Soc. 146 (6) (1999) 2092.

[43] G. Herzer, Journal of Magnetism and Magnetic Materials 112, 258-262 (1992)

[44] Y. J. Zhang, Z. Wang, K. Y. He, H. H. Zhao, L. Z. Cheng, H. C. Yang, Acta Metallurgica Sinica 14 (2001) 267-270.

[45] Eiichi Hirota, Journal of the Physical Society of Japan. Vol. 19, No. 1, January, 1964

[46]M. H. Seavey, Jr. and P. E. Tannenwald: J. appl. Phys. 30 (1959) 227S.

[47] Y. J. Zhang, Z. Wang, K. Y. He, H. H. Zhao, L. Z. Cheng, H. C. Yang, Acta Metallurgica Sinica 14 (2001) 267-270.

[48] Herr.A., Meyer. A. J. P., Journal of Applied Physics, 39, 669-670 (1968)

[49] O.S. Lutes, J.O. Holmen et al., IEEE Trans. Magn.MAG-13 (1977) 1615.

[50] Chin-An Chang, Appl. Phys. Lett. 57 (1990) 297.

[51] P. Poulopoulos, R. Krishnan et al., J. Magn. Magn. Mater.163 (1996) 27.

[52] C. Gao, M.J. O'Shea, J. Magn. Magn. Mater. 127 (1993)181.

[53] M.J. O'Shea, A.L. Al-Sharif, J. Appl. Phys. 75 (1994) 6673.

[54] C.A. dos Santos, B. Rodmacq, J. Magn. Magn. Mater. 147(1995) L250.

[55] K. Takanashi, H. Kurokawa, H. Fujimori, Appl. Phys.Lett. 63 (1993) 1585.

[56] X. Yan, Y. Xu, J. Appl. Phys. 19 (1996) 6013.

[57] A. Aharoni, J. Appl. Phys. 76 (1994) 6977.

[58] M. Tejedor, H. Rubio, A. FernaHdndez, Appl. Phys. Lett. 55 (1989) 1920.

[59] Barbara Szpunar, Uwe Erb, and Gino Palumbo, Physical Review B, Volume 53, Number 9, 5547-5556

[60]Aus, M.J., Cheung, C., Szpunar, B., Erb, U. and Szpunar, J.A., J. Mater. Sci. Lett., 17: 1949 (1998)

[61]Szpunar, B., Aus, M.J., Cheung, C., Erb, U., Palumbo, G., and Szpunar, J.A., J. Magn. Magn. Mater., 187:325 (1998).

[62] Cheung, C., Aus, M. J., Erb, U., McCrea, J.L., and Palumbo, G., in: Proc. 6th Int. Conf. Nanostruct. Mater., (NANO 2002), CD-ROM, Nanotechnology Enterprises Inc., Rutgers University, NJ (2003)

[63] Samuel Maquire-Boyle, Andrew R. Barron. Theory of a Superconducting Quantum Interference Device (SQUID)

[64] J. Bland Thesis M. Phys (Hons)., ‘ Amossbauer spectroscopy and magnetometry study of magnetic multilayers and oxides.’ Oliver Lodge Labs, Dept, Physics, University of Liverpool.

[65] B. D. Cullity, Introduction to Magnetic Materials, Addison-Wesley Publishing Company, Inc.: Reading, MA, (1972).